

Stress-Corrosion Cracking Characterization of High-Strength Steels— Base Metals and Weldments

C. T. FUJII, F. W. FRASER, and E. A. METZBOWER

Material Science and Technology Division

May 12, 1978



NAVAL RESEARCH LABORATORY
Washington, D.C.

Approved for public release; distribution unlimited.

SECURITY CLASSIFICATION OF THIS PAGE (When Data Entered)



CONTENTS

BACKGROUND	1
SCC TESTS AND RESULTS.....	1
Materials	1
PROCEDURES.....	3
SCC Results.....	5
HY-130 Base Metals	5
10Ni-8Co (HY-180) and 9Ni-4Co Base Metals.....	5
HY-130 Weld Metals	9
HY-180 Weld Metals (10Ni)	9
Summary.....	9
FRACTOGRAPHY, METALLOGRAPHY, AND HARDNESS MEASUREMENTS OF BASE-METAL SPECIMENS.....	10
Procedures.....	10
RESULTS.....	11
Code-A HY-130 Base Metal.....	11
Code-B HY-130 Base Metal.....	15
Code-C HY-130 Base Metal.....	18
Code-H HY-130 Base Metal.....	23
Plate-V HY-130 Base Metal.....	26
Code-E 10Ni-8Co (HY-180) Base Metal.....	28
Code-D 10Ni-8Co (HY-180) Base Metal	34
Code-G 9Ni-4Co Base Metal	39
Code-F 9Ni-4Co Base Metal	43
DISCUSSION	46
ACKNOWLEDGMENTS.....	46
REFERENCES	47
APPENDIX A — Chemical Composition and Tensile Properties of the Materials.....	48

STRESS-CORROSION-CRACKING CHARACTERIZATION OF HIGH-STRENGTH STEELS—BASE METALS AND WELDMENTS

BACKGROUND

This report summarizes the studies conducted by the Naval Research Laboratory during FY-1977 (1 October 1976 to 30 September 1977) under Tasks 1.4 and 1.3 in the High-Strength Steel Weldment Subcritical Cracking Program sponsored by the Naval Sea Systems Command (SEA 035) and managed by the Materials Department of the David W. Taylor Naval Ship Research and Development Center, Code 28, Annapolis, Maryland. The objectives of Tasks 1.4 and 1.3 were the characterization of the stress-corrosion-cracking (SCC) properties of selected materials in terms of an elastic fracture mechanics parameter and fracture modes. The effects of compositional, metallurgical, and microstructural changes induced by processing, welding, or heat treating on SCC sensitivities were determined, and analysis of correlations between microstructural features, fracture modes, and SCC properties were initiated. The studies were "baseline" studies on both base metals and weld metals in the 800-to-1400-MPa (110-to-200-ksi) yield-strength range and focused on identifying the most promising paths for subsequent more-intensive research.

The report is divided into two main sections. The first section covers the SCC test procedures and results; the second section describes the significant microstructural and fractographic features observed on the test specimens examined during the reporting period.

SCC TESTS AND RESULTS (by C. T. Fujii)

The test method adopted was designed to fulfill the task objective of distinguishing the SCC characteristics of base metals and weldments in terms of a parameter with engineering significance. Thus, in view of its proven reliability, the cantilever method was selected for determining K_{Isc} , which is the critical stress-intensity factor for environmental crack initiation. The normally lengthy test was modified to minimize experimental time and the number of specimens required. The data obtained by this procedure were considered to be entirely adequate to differentiate materials with superior SCC resistance from those which were intermediate or inferior.

Materials

The materials selected for the program and the test formats for the SCC studies are summarized in Figs. 1 and 2. An assigned letter code in brackets identifies each material and its condition. The detailed chemical compositions of these materials are given in Tables A1 and A2 of Appendix A, and the tensile properties are summarized in Tables A3 and A4.

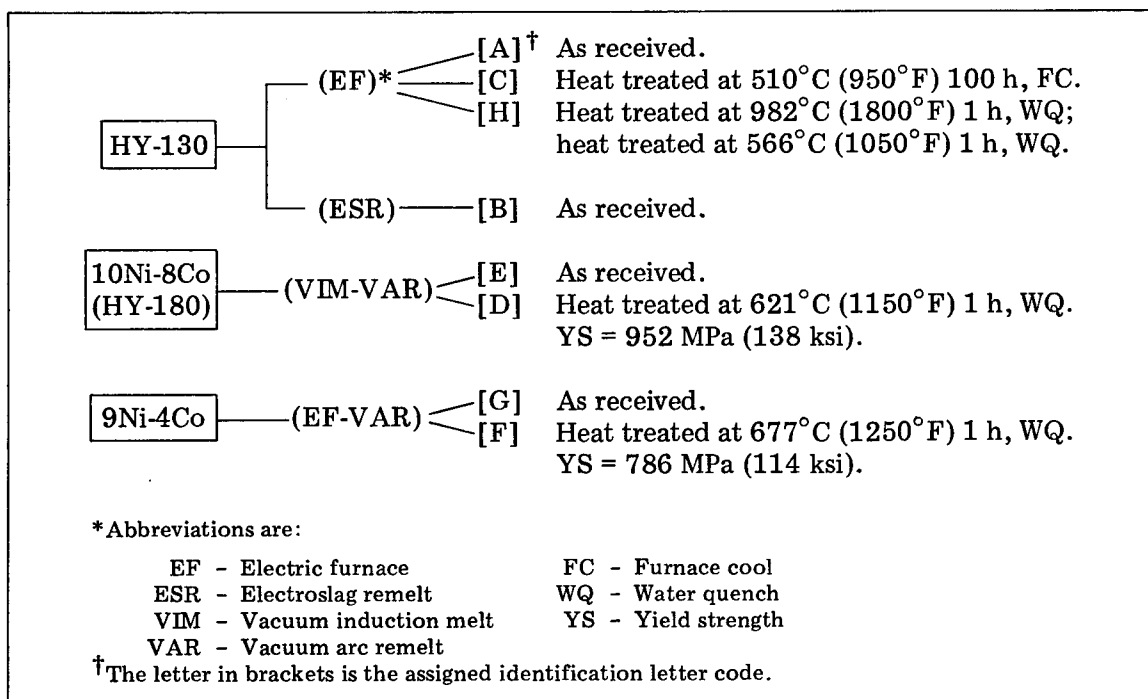


Fig. 1 — SCC test format for HY-130, 10Ni-8Co, and 9Ni-4Co base metals

Figure 1 lists the base metals and the heat treatments used to alter their metallurgical conditions. The base metals studied included two 25-mm-thick (1-in.-thick) HY-130 plates, a 38-mm-thick (1.5-in.-thick) 10Ni-8Co (HY-180) plate, and a 25-mm-thick (1-in.-thick) 9Ni-4Co plate. One HY-130 plate was processed by the electric furnace (EF) method and the other by electroslag remelt (ESR) practice. The 10Ni-8Co steel was produced by the vacuum-induction-melt/vacuum-arc-remelt (VIM-VAR) process, and the 9Ni-4Co steel was produced by the electric-furnace/VAR (EF/VAR) process. All base metals were tested in the as-received condition in full thickness. Additionally, all of the base metals, with the exception of the ESR HY-130 plate, were heat treated and reevaluated for SCC sensitivity.

The characterized weldments were all 38 mm thick (1.5 in. thick) in the HY-130 or HY-180 system. Figure 2 gives the complete test format arranged according to the combination of base metal and filler material (electrode material) used and the welding procedure used. For studies in the HY-130 system, three welding procedures were used: the gas metal arc (GMA), gas tungsten arc (GTA), and shielded metal arc (SMA). One of four different electrodes was used in the fabrication of HY-130 weldments: Airco, Linde, Matching Composition, and McKay. The HY-180 weldments were made by the GTA process using filler material with a composition similar to that of the base metal (10Ni-8Co) and either a normal or a high heat input. As outlined in the test format of Fig. 2, some of the welds in the two systems were subjected to postweld heat treatments and tested in these conditions.

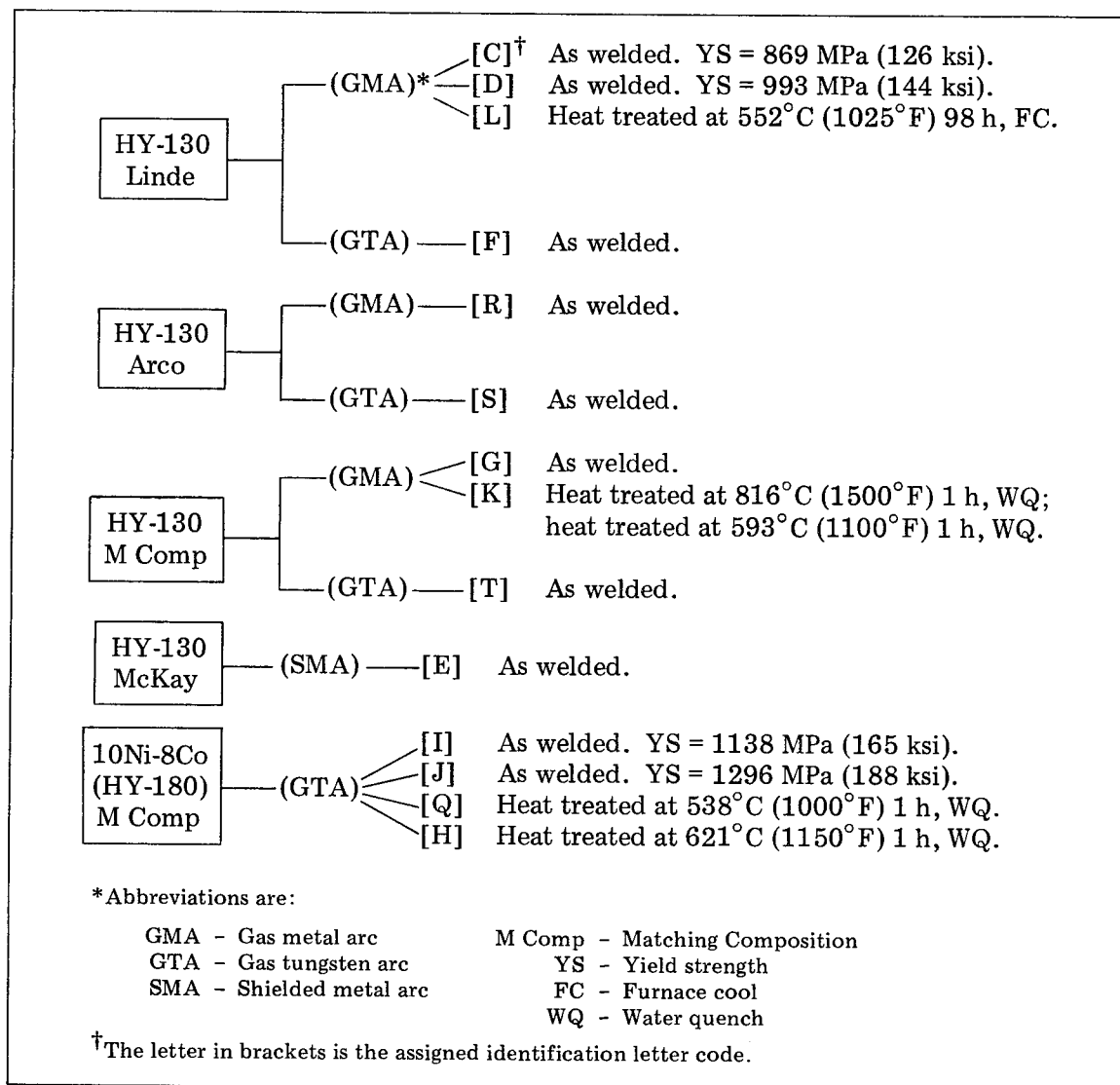


Fig. 2 — SCC test format for HY-130 and HY-180 weld metals

PROCEDURES

Single-edge-notched fatigue-precracked specimens illustrated in Fig. 3a and the cantilever beam method described by Brown [1] and illustrated in Fig. 3b were used to evaluate the SCC characteristics of the selected materials. The Kies equation—given in the lower portion of Fig. 3a, where M is the moment and a , W , and B are the crack length, height, and thickness of the specimen—was used to calculate the threshold stress-intensity factors [2]. The experiments on the 25-mm-thick (1-in.-thick) specimens (HY-130 and 9Ni-4Co plates) were conducted on a conventional weight-loaded cantilever beam as depicted in Fig. 3b. The 38-mm-thick (1.5-in.-thick) specimens (10Ni-8Co (HY-180) plate) which required heavier loads were tested in the hydraulically loaded system shown in Fig. 4 [3].

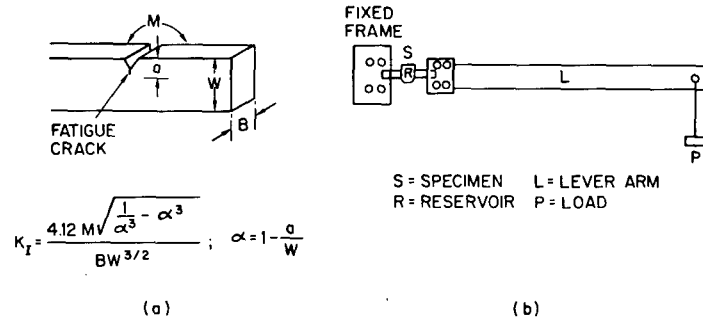


Fig. 3 — Schematic of (a) fatigue-precracked cantilever specimen and (b) cantilever test equipment for measuring K_{Isc}

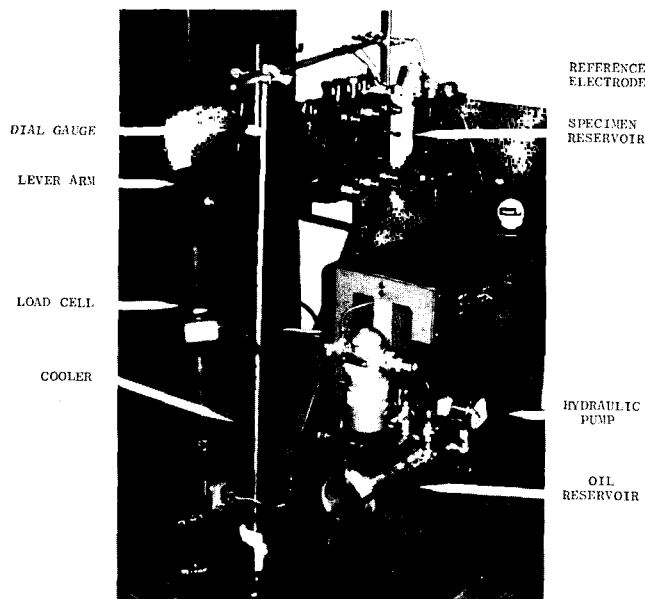


Fig. 4 — NRL hydraulic cantilever test system

The stress-intensity factors for fast fracture in air K_{I_x} were first measured on a specimen of each material and subsequently used to guide load settings for the K_{Isc} tests on another specimen of each material. The initial loads for the K_{Isc} tests were usually 40 to 50 percent of that used to establish K_{I_x} values. To determine the critical K_I value for saltwater crack growth, a step-loading bracketing technique was used. Loads were increased incrementally every 100 hours until crack growth was observed. Each load increment corresponded to an increase in K of approximately $11 \text{ MPa} \cdot \text{m}^{1/2}$ ($10 \text{ ksi} \cdot \text{in.}^{1/2}$). Indications of crack growth were obtained by noting the movement of the cantilever beam via a precision dial gage positioned near the loaded end of the beam. Upon completion of each SCC test, stress-corrosion crack growth was verified by visual and microscopic examination of the fracture surfaces. The critical K_I value K_{Isc} was considered to be bracketed between the K_I

which produced crack growth and fracture and the highest K_I which failed to cause any crack extension after 100 hours. Thus $K_{I_{SCC}}$ was determined by averaging the K_I values associated with the final two loads.

All of the SCC tests were conducted in nonflowing 3.5-percent sodium chloride (NaCl) solution with the specimens coupled to zinc anodes and at ambient temperature of approximately 24°C. The salt solution was changed each work day.

SCC Results

The results of the cantilever tests are given in Table 1 for the base metals and in Table 2 for the weld metals. Included in the data summation are some details of the SCC tests including (last three columns) the number of loading increments, the time required for crack initiation at the final load, and the elapsed time for stress-corrosion crack growth at the final load preceding the terminal event of fast fracture. In view of the short hold times (approximately 100 hours) between load increments in the SCC tests, $K_{I_{SCC}}$ is employed only as a ranking index at this time and thus is put in quotation marks. It is used in these studies to rate those factors which influence the SCC properties in order to aid in charting directions for effecting improved weld metal performance. Conventionally, longer hold times are recommended to obtain $K_{I_{SCC}}$ data which are valid and acceptable for use in any precise analysis based on elastic fracture mechanics.

The " $K_{I_{SCC}}$ " data are plotted versus the yield strength in Fig. 5 for the base metals and in Fig. 6 for the weld metals to facilitate comparisons of the SCC behavior of the precracked specimens. The position of the data points relative to the grid of constant ratio lines is used to rank the SCC resistance of the materials tested. Thus higher ratio materials are considered to be superior to lower ratio materials unless a cracking mechanism other than SCC is indicated by examination of the fracture surfaces. The following interpretations and conclusions concerning the SCC properties of base and weld metals determined in these studies are arrived at on this premise.

HY-130 Base Metals

- Both ESR (code B) and EF (code A) processed materials had relatively good SCC resistance; the difference in SCC behavior between the two under these experimental conditions was small.
- Heat treatment which produced embrittlement (code C) or coarse-grain microstructure (code H) increased the SCC sensitivity of the base metal.

10Ni-8Co (HY-180) and 9Ni-4Co Base Metals

- The SCC properties of the 10Ni-8Co steel (codes E and D) were superior to that of 9Ni-4Co steel (codes G and F).
- Heat treatment of the 10Ni-8Co steel to produce a lower-yield-strength material (code D) within the range of HY-130 resulted in a large improvement in SCC resistance.

Table 1 — SCC Properties of the Base Metals

Material*	Code	Condition	Yield Strength		K _{IX} , air		"K _{Isc} , Zn"		No. of Loads	Initiate [†] (h)	Fracture [†] (h)
			(MPa)	(ksi)	(MPa·√m)	(ksi·√in.)	(MPa·√m)	(ksi·√in.)			
HY-130 (EF)	A	As received	938	136	190	173	101	92	3	0.4	120.0
HY-130 (ESR)	B	As received	986	143	176	160	112	102	3	0.4	20.6
HY-130 (EF/TE)	C	Heat treated	910	132	158	144	97	88	2	0.3	1.3
HY-130 (EF/CG)	H	Heat treated	1027	149	187	170	90	82	2	0.9	142.5
10Ni-8Co (HY-180)	E	As received	1282	186	179	163	132	120	5	24.0	234.7
10Ni-8Co (HY-180)	D	Heat treated	952	138	207	188	138	126	4	24.0	73.2
9Ni-4Co	G	As received	1282	186	184	167	85	77	4	0.2	149.9
9Ni-4Co	F	Heat treated	786	114	140	127	79	72	3	0.5	43.2

*EF - electric furnace,
 ESR - electroslog remelt,
 TE - temper embrittled,
 CG - course grain.

[†]Elapsed time at final load in the SCC test.

Table 2 — SCC Properties of the Weld Metals

Material/ Electrode	Weld [†]	Code	Condition	Yield Strength		K _{IX} , air		“K _{Isc} , Zn”		No. of Loads	Initiate [‡] (h)	Fracture [‡] (h)
				(MPa)	(ksi)	(MPa·√m)	(ksi·√in.)	(MPa·√m)	(ksi·√in.)			
HY-130 Linde	GMA	C	As welded	869	126	184	167	91	83	3	6.5	22.5
		D	As welded	993	144	209	190	90	82	3	30.2	91.9
		L	Heat treated	1000	145	56	51	42	38	5	24	57.6
		F	As welded	1041	151	244	222	99	90	4	3	31.0
		F' [§]						113	103	4	3	74.3
HY-130 Airco	GMA	R	As welded	1034	150	154	140	109	99	2	22.5	47.1
		S	As welded	1041	151	201	183	108	98	2	2.4	51.4
HY-130 M Comp	GMA	G	As welded	938	136	135	123	101	92	2	1.5	20.1
		K	Heat treated	903	131	153	137	123	112	3	≈0.6	0.8
		T	As welded	1048	152	226	206	126	115	3	6.6	27.2
HY-130 McKay	SMA	E	As welded	993	144	154	140	110	100	2	2	27.7
10Ni-8Co M Comp	GTA	H	Heat treated	862	125	225	205	130	118	4	1	15.5
		I	As welded	1138	165	197	179	88	80	2	3	181.1
		J	As welded	1296	188	222	202	89	81	2	18	170.8
		Q	Heat treated	1331	193	245	223	104	95	2	50	180.0

*M Comp - Matching composition.

[†]GMA - gas metal arc.

GTA - gas tungsten arc.

SMA - shielded metal arc.

[‡]Elapsed time at final load in the SCC test.[§]Specimen thickness B reduced from 38 to 25 mm.

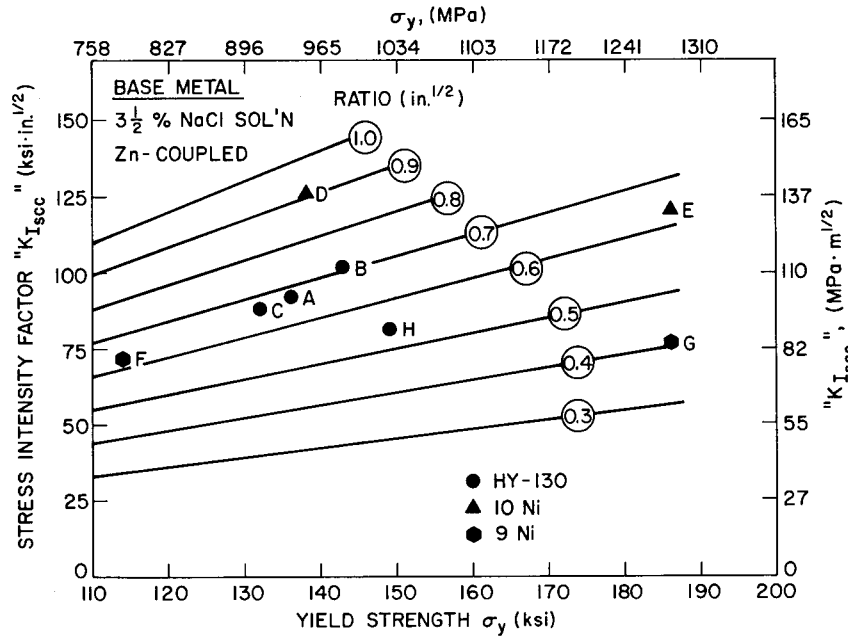


Fig. 5 — Ranking of the SCC resistance of the HY-130, 10Ni-8Co, and 9Ni-4Co base metals by comparison of ratios

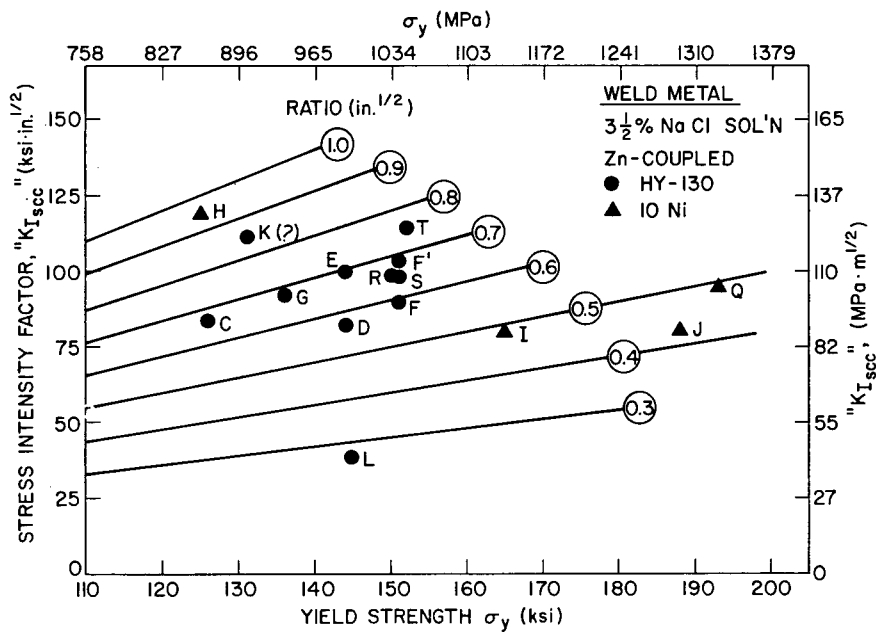


Fig. 6 — Ranking of the SCC resistance of the HY-130 and HY-180 weld metals by comparison of ratios

HY-130 Weld Metals

- The SCC behavior of the GMA and SMA as-welded materials was similar. As indicated by the results in Fig. 6, weldments prepared with the code-R Airco, code-G Matching Composition, and code-E McKay filler materials appeared to be slightly more resistant to SCC than the code-D Linde weld metal. The lower-yield-strength code-C Linde material exhibited a modest improvement in SCC resistance as seen in Fig. 6 by the shift toward the higher (0.7) ratio line.

- Within any given electrode system the GTA process produced a more SCC resistant weld metal than GMA. Additionally, a large variation in through-thickness properties was indicated by the pronounced concaveness of the stress-corrosion crack front on the fracture surfaces of the GTA materials, and the results of retesting of one of these—the code-F GTA weld metal—after removal of the more susceptible outermost material from opposing faces of the cantilever specimen demonstrated an even better SCC performance, as shown by the code-F' point in Fig. 6. The code-S and code-T GTA welds would be expected to respond similarly to tests on reduced-section specimens.

- Postweld heat treatments of the code-K Matching Composition and code-L Linde GMA weldments embrittled both materials and led to questionable SCC behavior. The code-K weld metal revealed limited crack growth which could not be unequivocally verified as SCC by examination of the fractures. The SCC properties (and the mechanical properties) of the code-L weld metal was decidedly inferior to all others in these studies.

HY-180 Weld Metals (10Ni)

- As a consequence of higher yield strength the code-I and code-J as-welded 10Ni filler materials were both less resistant to SCC than any of the as-welded HY-130 weld metals.

- Heat treatment to a lower yield strength (code H) improved the SCC resistance of the 10Ni filler material significantly. Tempering to a higher-yield-strength overaged condition (code Q) improved the SCC properties slightly relative to the as-welded condition.

- Extensive crack branching occurred in the 10Ni weld metal during the SCC tests.

Summary

The SCC tests have shown that tempering which produced embrittlement or coarse-grain microstructure slightly reduced the SCC resistance of HY-130 base metal and that the GTA welding process which produced a weldment characterized by fine beads and a small-grain microstructure gave the most SCC resistant weld metals. Weld metal composition in the HY-130 system did not appear to have a primary influence on SCC properties.

The experimental observations suggest that the 10Ni-8Co (HY-180) steel system may be more sensitive to hold time and incubation effects in SCC tests than the HY-130 base and weld metals. The 10Ni weld metal was also characterized by a greater propensity for macro

crack branching, another manifestation of the differences in SCC behavior of the two systems observed in these studies.

Although useful for a relative ranking of the SCC behavior of materials, the " K_{Isc} " values obtained in these studies should be regarded as approximations and used accordingly. As noted previously, valid parameters—if required—need to be established by conventional K_{Isc} test procedures. It should also be recalled that the SCC tests were conducted under zinc-coupled conditions in a saltwater environment which polarized the specimen at -1.0 V as measured against the Ag/AgCl reference electrode. The preponderance of evidence indicates that there is a significant and varying influence of potential on SCC properties and that increasing negative potentials generally decrease the SCC threshold of precracked steel specimens [4,5]. Thus, the present results are approximately representative of lower bound SCC behavior of the steels and weld metals in a saltwater environment, and more modest applied cathodic potentials would likely enhance the SCC resistance of the tested materials.

FRACTOGRAPHY, METALLOGRAPHY, AND HARDNESS MEASUREMENTS OF BASE-METAL SPECIMENS (by F. W. Fraser and E. A. Metzbower)

This second main section of this report is concerned with the fractography, metallography, and hardness of the base-metal materials (Tables A1 and A3). Each specimen is identified by assigned letter code as explained in Fig. 1, with the exception of plate V, an electric furnace steel. This material had been tested previously for stress-corrosion cracking and because of the high K_{Isc} range reported, 135 to 138 $\text{MPa}\cdot\text{m}^{1/2}$ (123 to 125 $\text{ksi}\cdot\text{in.}^{1/2}$) [4], fractographic and metallographic studies were carried out and are included in this report along with the hardness value. As indicated in Table 1, K_{Ix} , the stress-intensity factor for fast fracture in air was measured for a specimen of each material. However only the air-break specimen of the code-E material was included in this part of the investigation.

Procedures

The fracture surfaces were stripped with replicating tape and cleaned ultrasonically prior to fractographic studies in the scanning electron microscope. Areas of the specimens surveyed included SCC regions, fast-fracture regions, fatigue/SCC interfaces, and SCC/fast-fracture interfaces.

After completion of the fractographic studies, each specimen was cross-sectioned longitudinally, mounted, polished, and etched with 1-percent Nital, and the microstructure was identified optically.

Hardness values were measured with a Vickers microhardness tester under a 300-g load, and the results were converted to the Rockwell C scale.

RESULTS

The fractography, metallography, and hardness results were as follows.

Code-A HY-130 Base Metal

Cleavage was the predominant fracture mode in the SCC area in the code-A specimen (Fig. 7). Microvoid coalescence (MVC) was found in isolated regions within the SCC area with, the greatest incidence occurring in the vicinity of the fatigue/SCC interface (Fig. 8).

A relatively deep and continuous secondary crack was found along the fatigue/SCC interface (Fig. 9), and short, shallow secondary cracks were found throughout the SCC area, as seen in Fig. 7.

The SCC/fast-fracture interface showed cleavage and scattered patches of MVC, and the fast-fracture area exhibited MVC exclusively (Fig. 10).

A tempered martensitic microstructure of nonuniform grain size with grains ranging from coarse to fine on a relative scale was found throughout (Fig. 11).

Microcracking was found only at the fracture edge and only in the form of short secondary cracks. The largest of these was seen at the fatigue/SCC interface (Fig. 12) and coincided in location with that seen on the fracture surface (Fig. 9).

The hardness was 31 Rc.

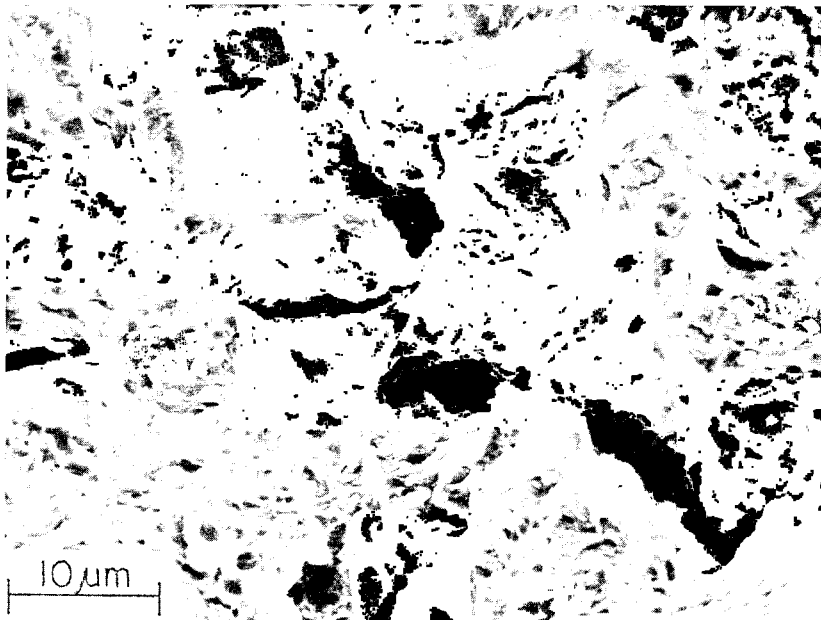


Fig. 7 — Code-A specimen: SCC area showing cleavage and short secondary cracks

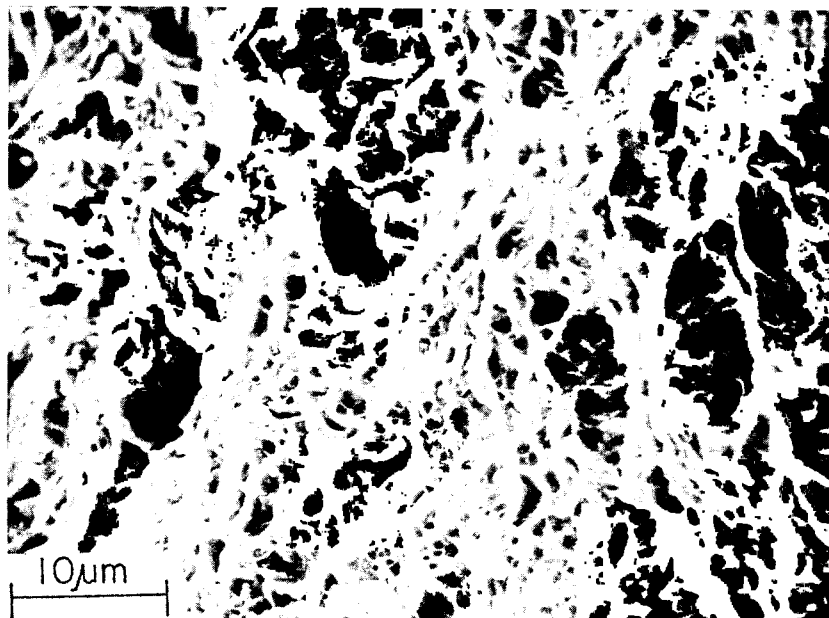


Fig. 8 — Code-A specimen: SCC area in the vicinity of the fatigue/SCC interface showing microvoid coalescence (MVC)

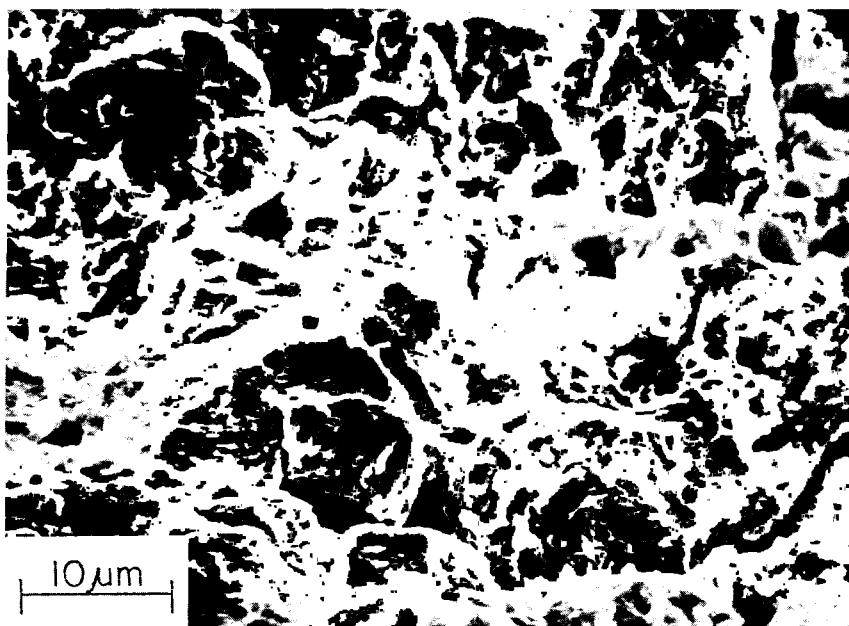


Fig. 9 — Code-A specimen: secondary crack at the fatigue-SCC interface

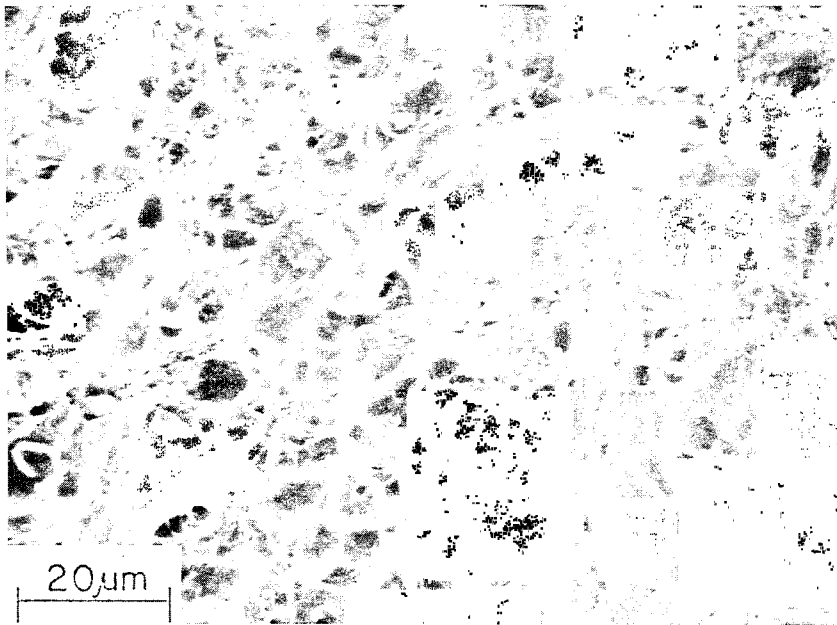


Fig. 10 — Code-A specimen: fast-fracture area showing MVC

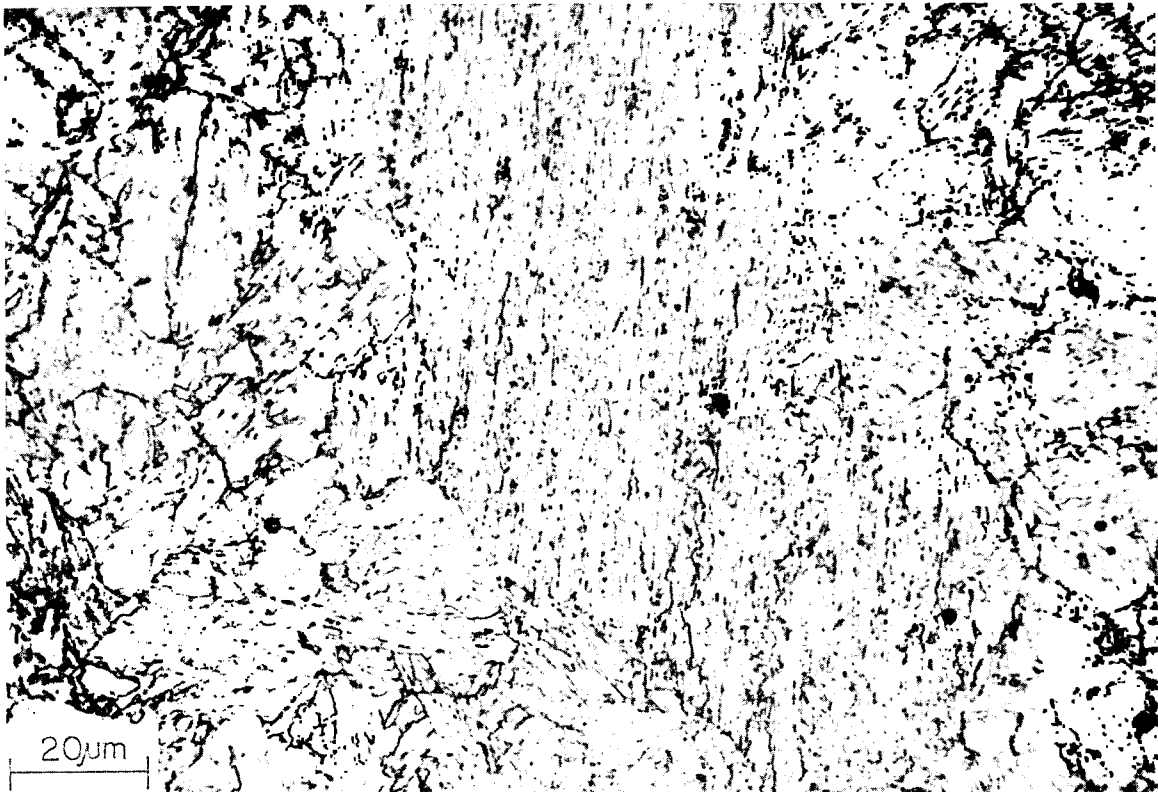


Fig. 11 — Code-A specimen: area showing tempered martensite of nonuniform grain size

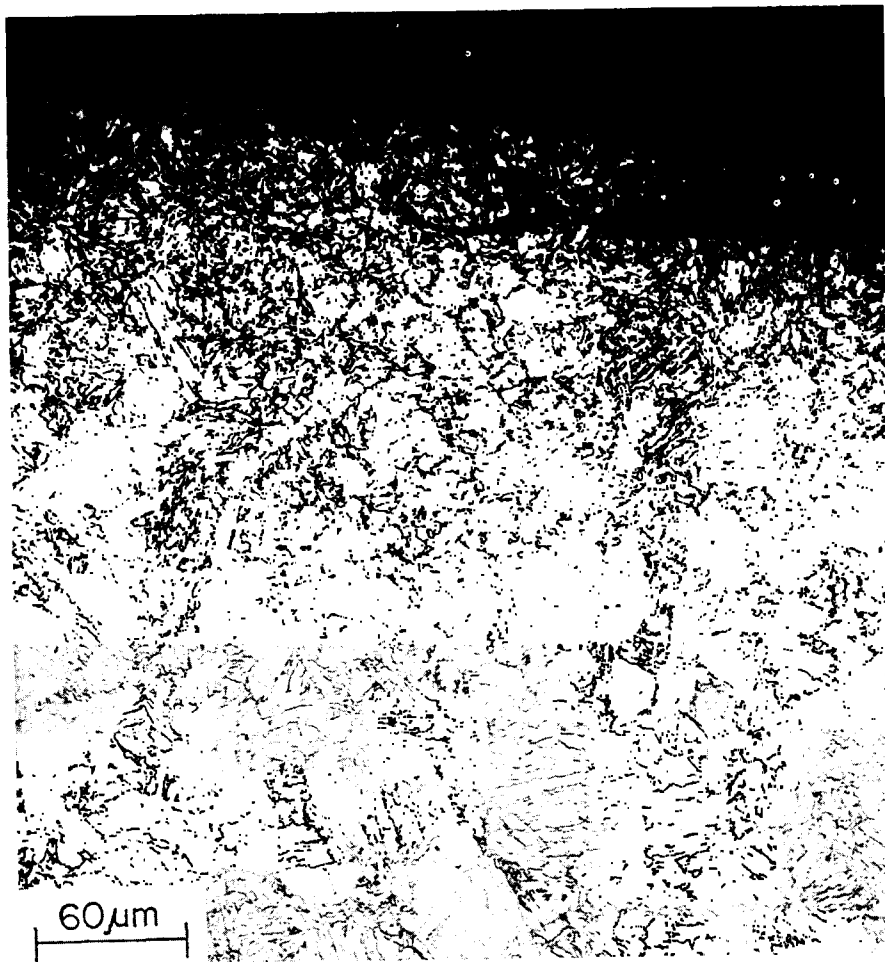


Fig. 12 — Code-A specimen: secondary crack at the fatigue/SCC interface

Code-B HY-130 Base Metal

MVC characterized the fracture surface of the code B specimen. All areas surveyed exhibited fine equiaxed dimples with some stretching throughout the SCC area and some evidence of pitting.

Although relatively little secondary cracking was found at the fatigue/SCC interface, as seen in Fig. 13, secondary cracking did occur in localized areas in the SCC region, and these areas showed fracture by cleavage (Fig. 14a). Smooth, featureless formations were found scattered across the fracture surface and can be seen in the SCC area in Fig. 14b as irregular or elongated shapes. Figure 14b is a higher magnification micrograph of the formations located at the center of Fig. 14a. In the fast-fracture area these formations appeared as a more or less regular donut shape or as spherical particles (Fig. 15).

The microstructure was composed of tempered martensite of a relatively uniform grain size (Fig. 16). Microcracking was found only in the form of short secondary cracks at the fracture edge. No extensive secondary cracking was seen at the fatigue/SCC interface.

The hardness was 33 Rc.

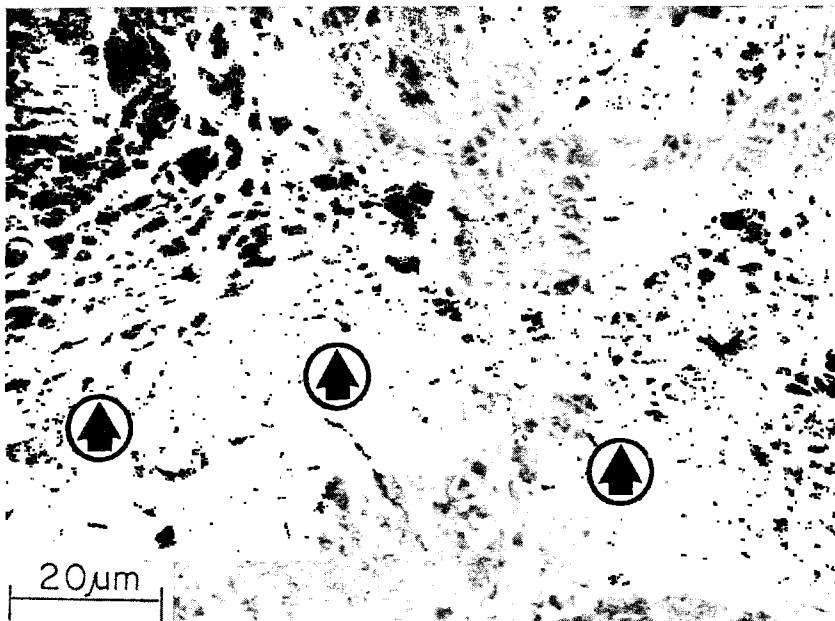


Fig. 13 — Code-B specimen: fatigue/SCC interface (arrows), with MVC in the SCC area above the interface and relatively little secondary cracking

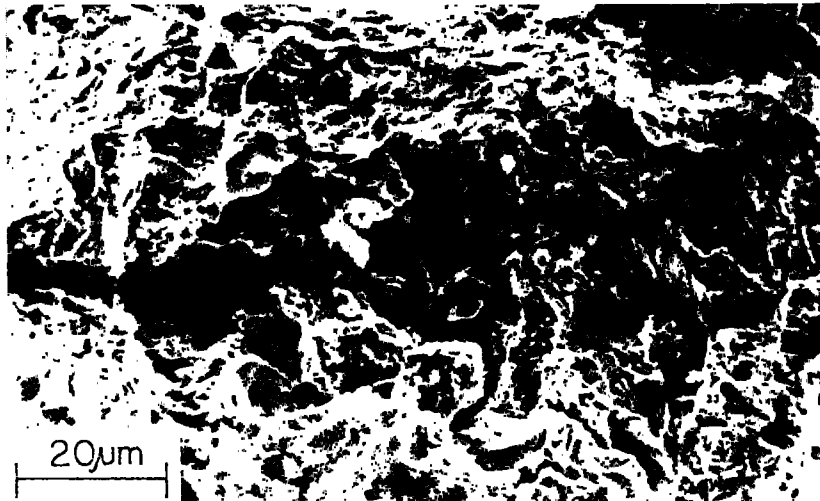


Fig. 14a — Code-B specimen: secondary cracks in a localized area showing fracture by cleavage in the SCC area

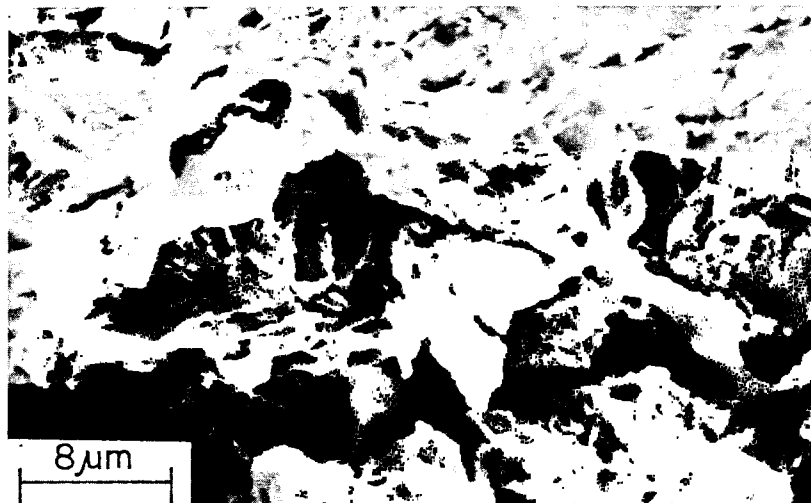


Fig. 14b — Smooth, featureless formation seen at the center of Fig. 14a

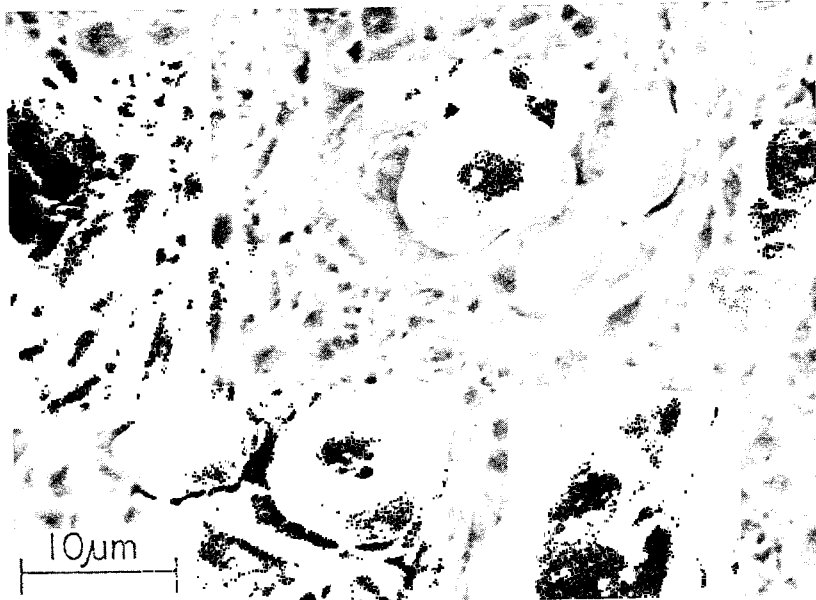


Fig. 15 — Code-B specimen: donut-shaped formations and spherical particles found in the fast-fracture area

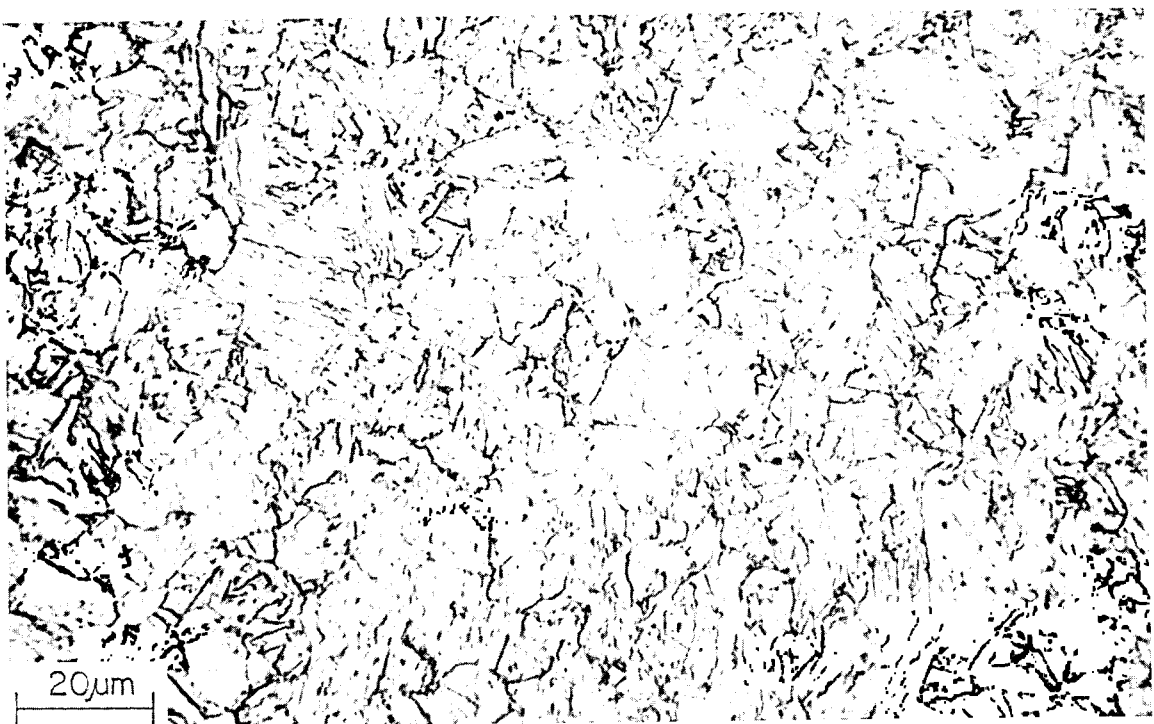


Fig. 16 — Code-B specimen: tempered martensite of uniform grain size

Code-C HY-130 Base Metal

An extremely shallow SCC zone extending a maximum of about 5 mm from the fatigue/SCC interface along the fracture surface was found in the code-C specimen. The fracture mode at the interface and in the SCC area was cleavage (Fig. 17). The fast-fracture area showed cleavage and MVC (Fig. 18).

Extensive secondary cracking had taken place along the fatigue/SCC interface (Fig. 19). In general, secondary cracks found on the fracture surfaces of the specimens analyzed propagated transverse to the direction of primary crack propagation. In the code-C specimen however numerous short secondary cracks were found running parallel to the direction of the primary crack (Fig. 20). A polished and etched, transverse cross section of this specimen showed heavy, irregular banding (Fig. 21). A hardness value of 37 Rc was found in the dark etched bands, and a value of 31 Rc was found in the matrix. The longitudinal secondary cracks seen on the fracture surface are probably associated with the banding. Similar transverse cross sections of codes A and H showed very fine uniform banding with no significant variations in hardness between the darker etched bands and the lighter etched matrices.

The microstructure of the code-C specimen was composed of tempered martensite with areas of spheroidized carbides (Fig. 22).

A deep secondary crack which was found at the fatigue/SCC interface (Fig. 23) correlated with the extensive secondary cracking seen along the fatigue/SCC interface on the fracture surface in Fig. 10.

The hardness was 31 to 37 Rc.

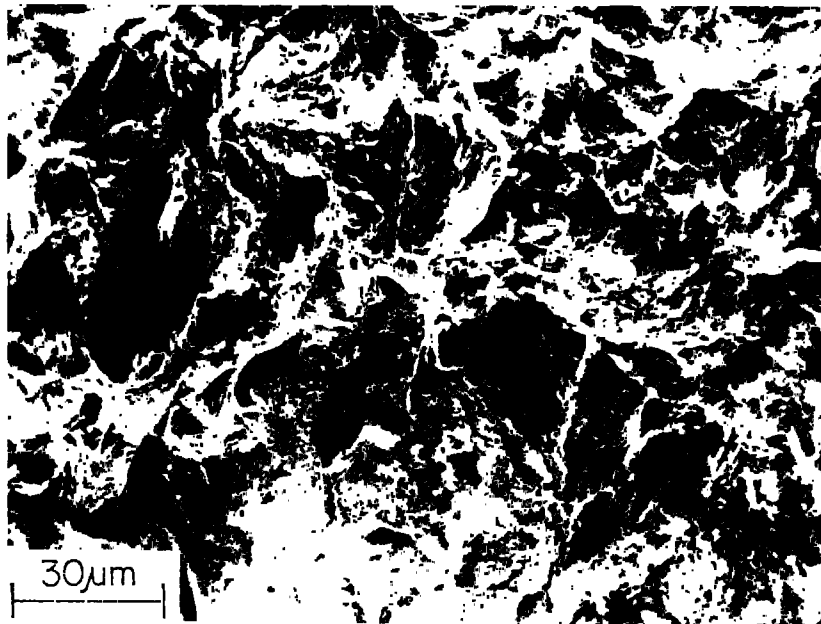


Fig. 17 — Code-C specimen: SCC area showing fracture by cleavage

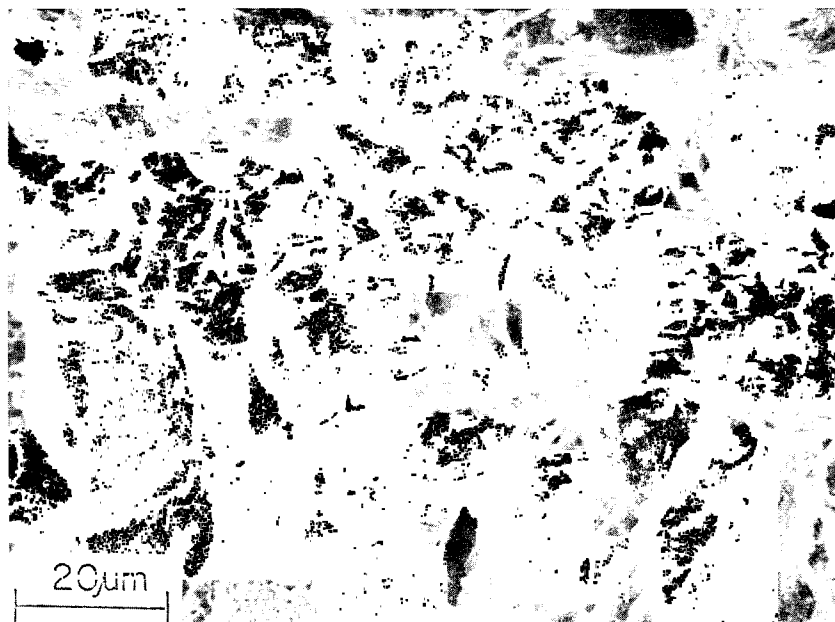


Fig. 18 — Code-C specimen: fast-fracture area showing cleavage and MVC

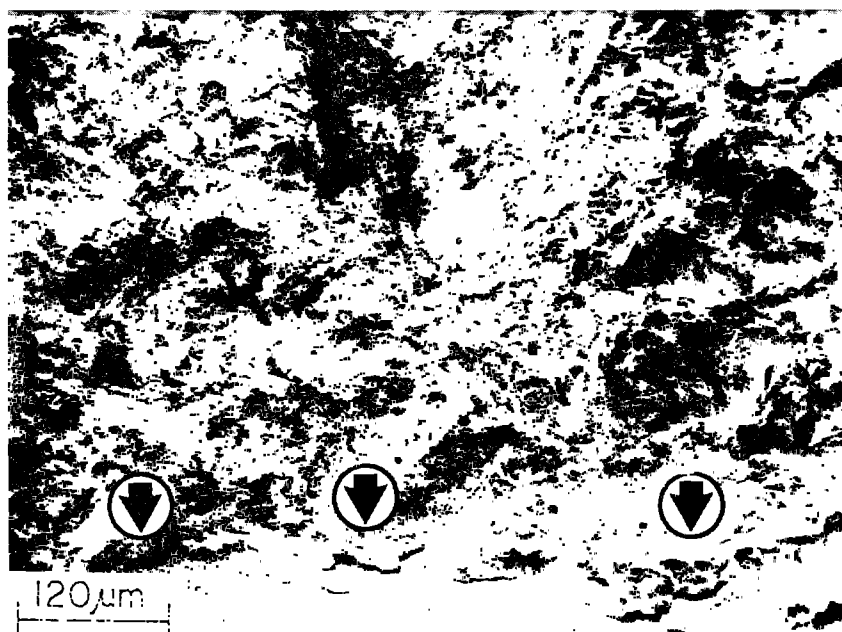


Fig. 19 — Code-C specimen: secondary cracking along the fatigue/SCC interface (arrows)

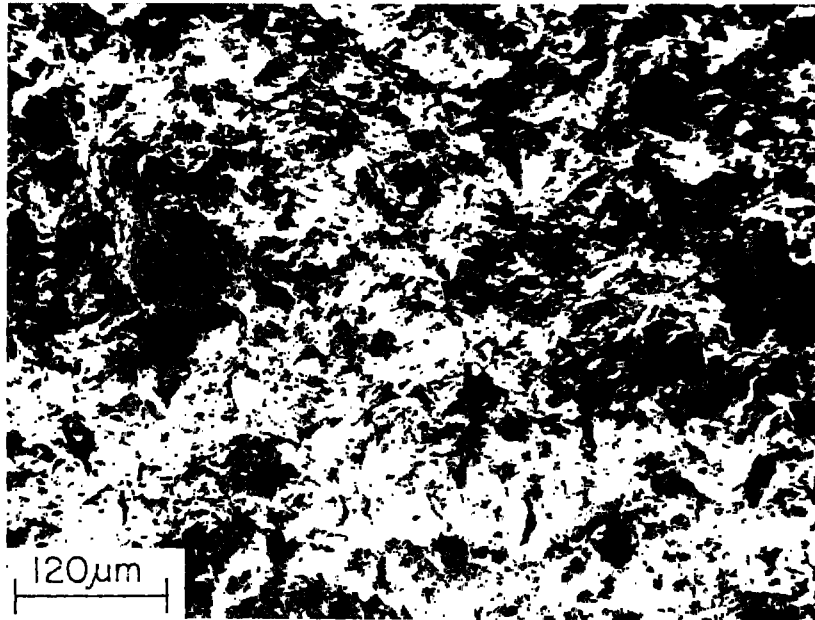


Fig. 20 — Code-C specimen: secondary cracks running parallel to the direction of primary crack propagation

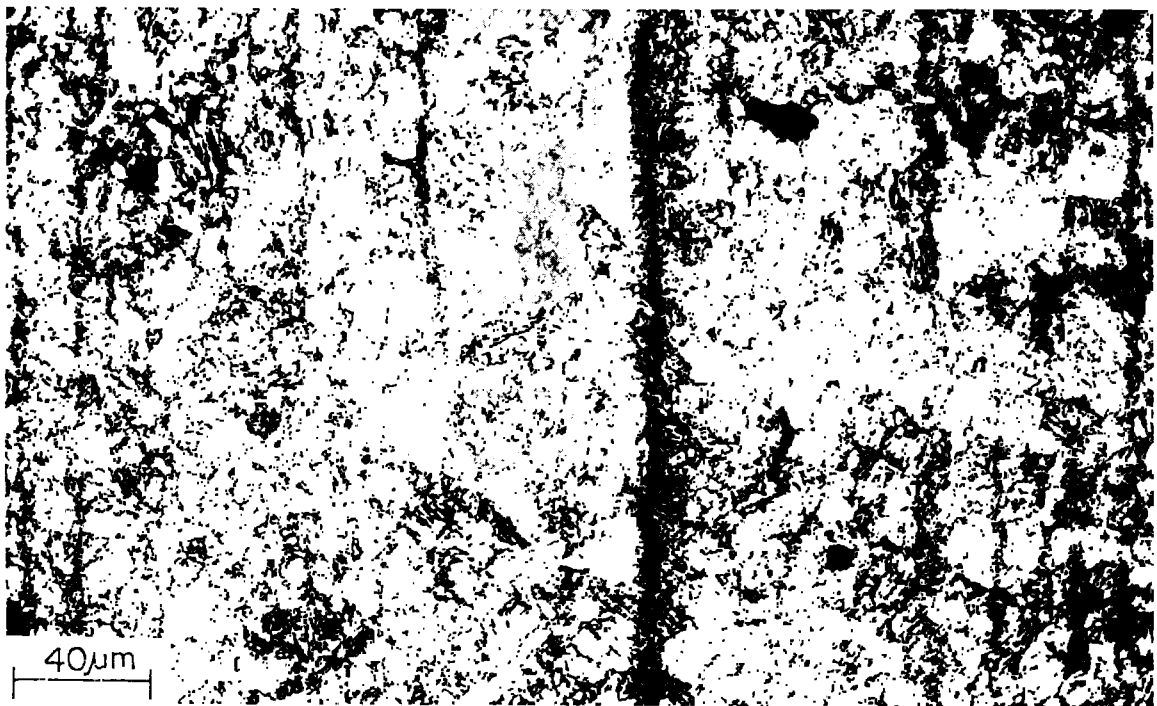


Fig. 21 — Code-C specimen: irregular banding seen in the transverse cross section

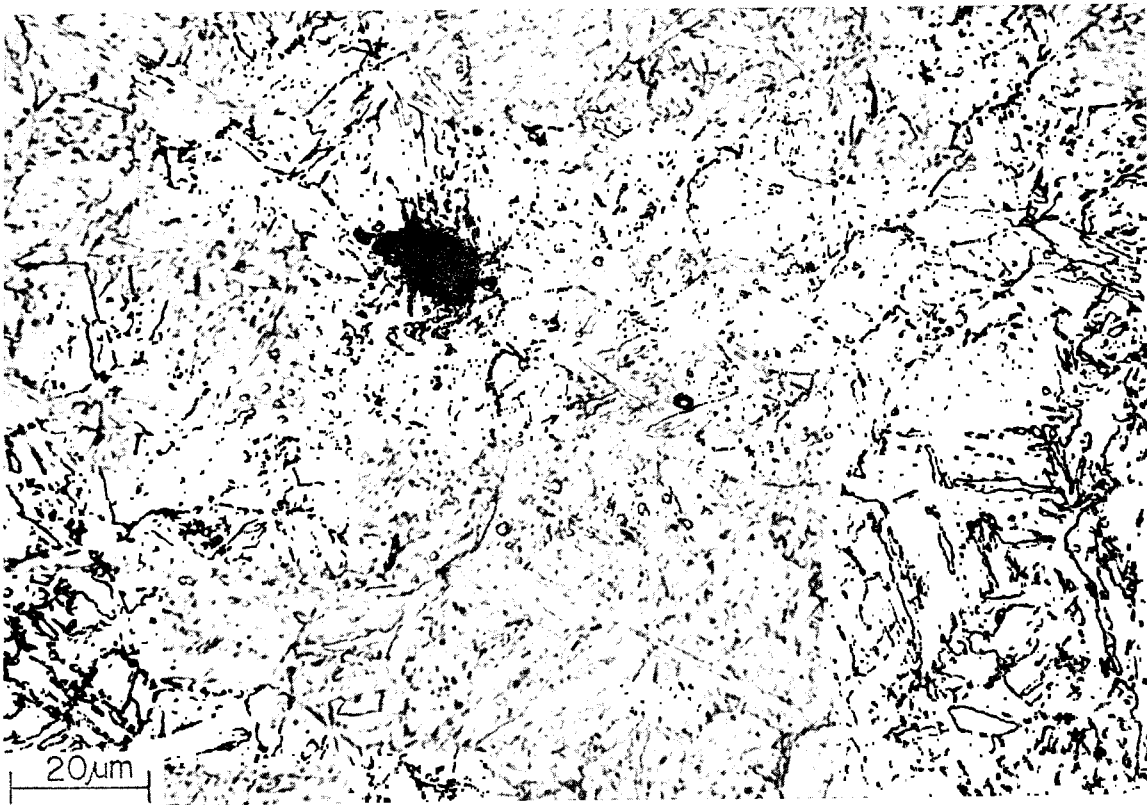


Fig. 22 — Code-C specimen: tempered martensite containing spheroidized carbides

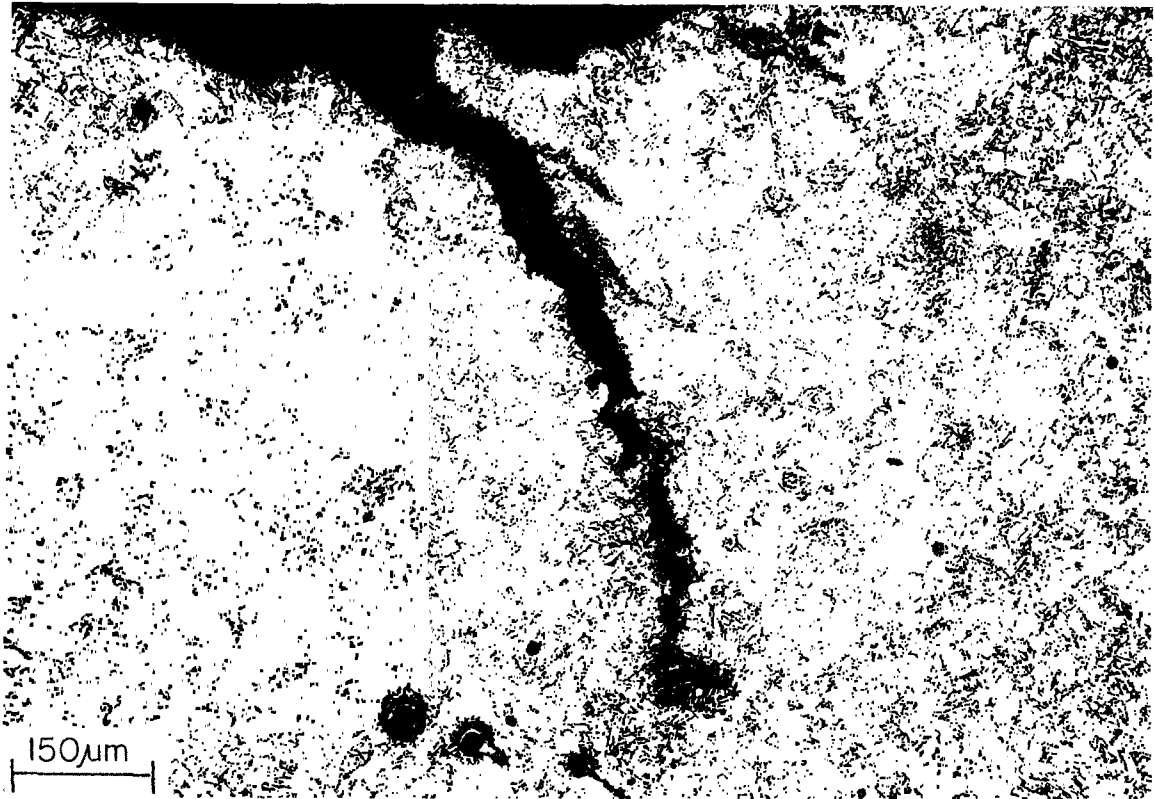


Fig. 23 — Code-C specimen: secondary crack at the fatigue/SCC interface

Code-H HY-130 Base Metal

As in the code-A and code-C specimens, extensive secondary cracking at the fatigue/SCC interface and in the SCC area had occurred in the code-H specimen (Fig. 24).

A mixed mode of intergranular fracture and cleavage was found in both areas, as seen in Fig. 25. In the fast-fracture area, fracture occurred by MVC (Fig. 26).

The microstructure was composed of tempered martensite (Fig. 27) slightly coarser in appearance and of a less uniform grain size than that seen in code C (Fig. 22). No evidence of spheroidization was found.

The hardness was 36 Rc.

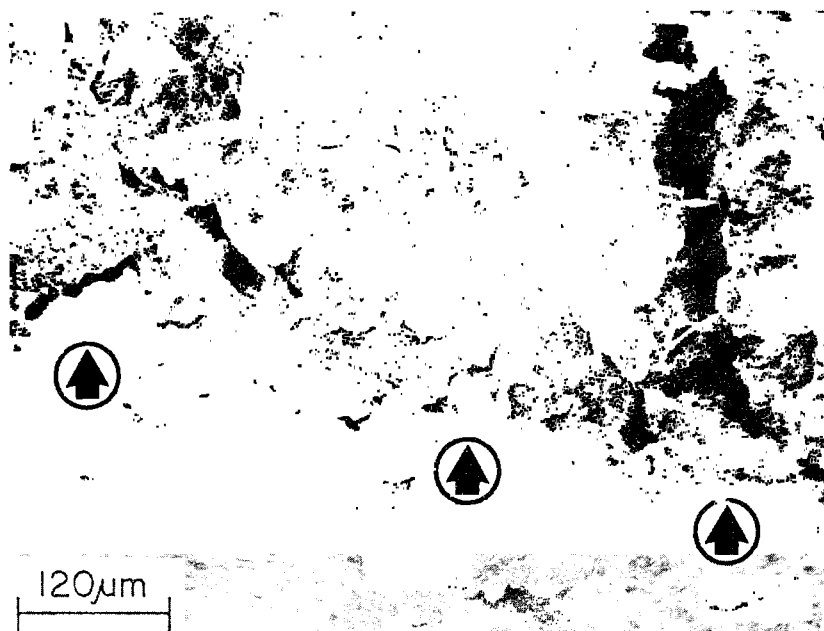


Fig. 24 — Code-H specimen: extensive secondary cracking at the fatigue/SCC interface (indicated by arrows) and in the SCC area (upper portion of the micrograph)

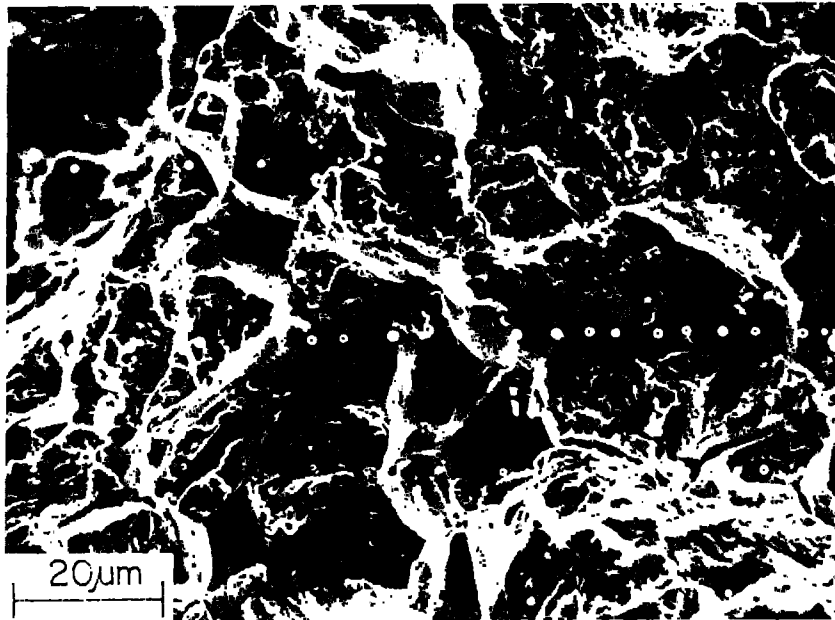


Fig. 25 — Code-H specimen: mixed intergranular fracture and cleavage in the SCC area near the fatigue/SCC interface

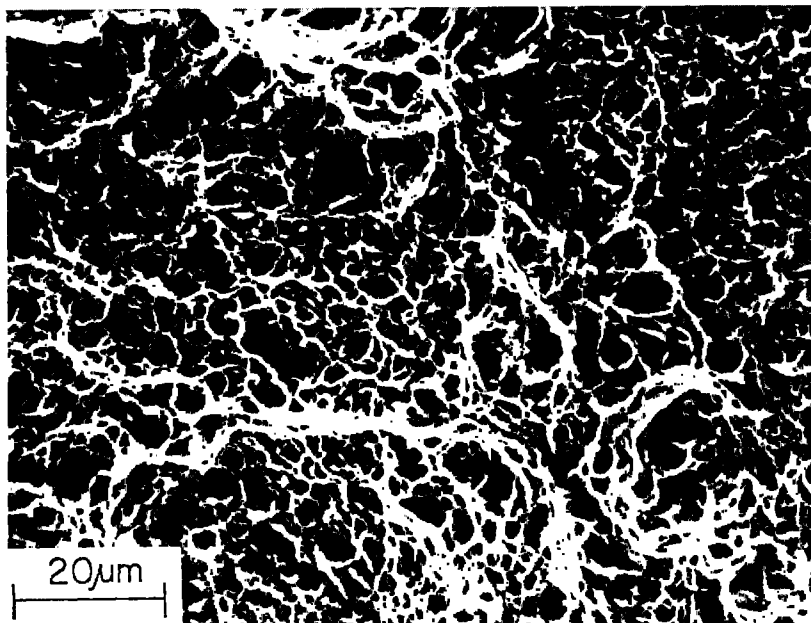


Fig. 26 — Code-H specimen: fast-fracture area showing MVC

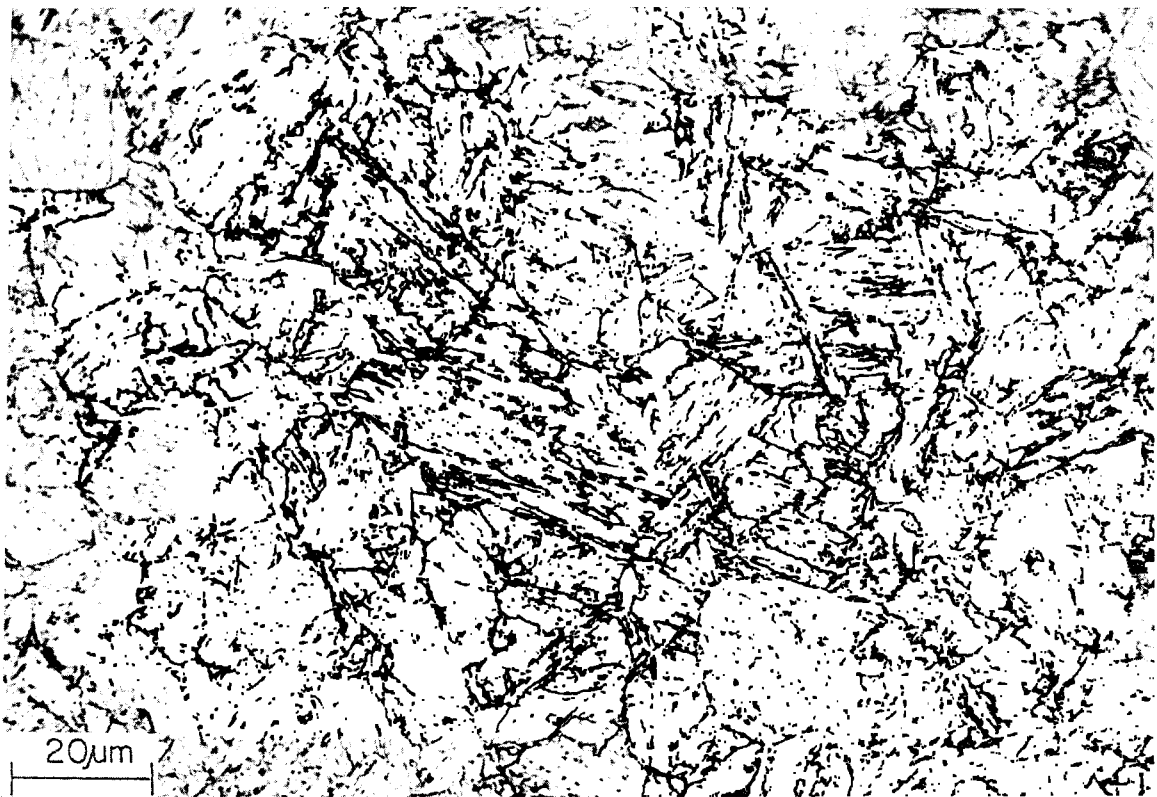


Fig. 27 — Code-H specimen: tempered martensite of a slightly coarser structure and a less uniform grain size as compared to that of the Code-C specimen (Fig. 22)

Plate-V HY-130 Base Metal

The mode of fracture, which in the plate-V specimen, was determined from stereo pairs taken by transmission electron microscopy rather than in the scanning electron microscope, was predominately MVC (Fig. 28), although minor amounts of cleavage (Fig. 29) had occurred in the SCC area. Some cleavage was also found in the fast-fracture area, although again fracture was predominately by MVC.

A tempered martensitic microstructure of a relatively uniform grain size and containing spheroidized carbides was found throughout (Fig. 30).

The hardness was 31 Rc.



Fig. 28 — Plate-V specimen: transmission-electron-microscope fractograph of the SCC area showing MVC

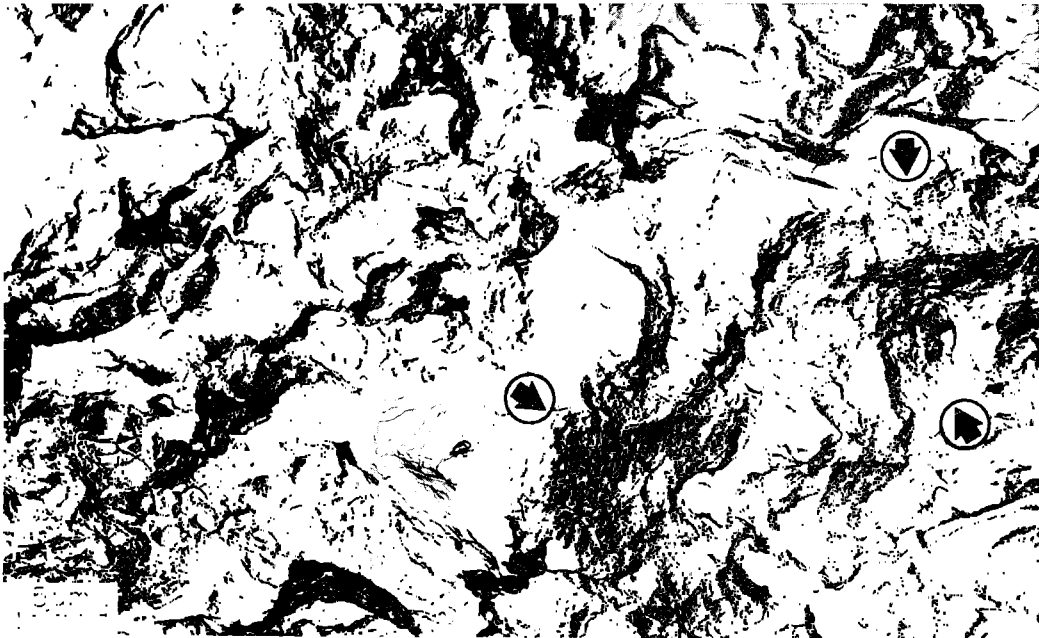


Fig. 29 — Plate-V specimen: transmission-electron-microscope fractograph of the SCC area showing small patches of cleavage (arrows)

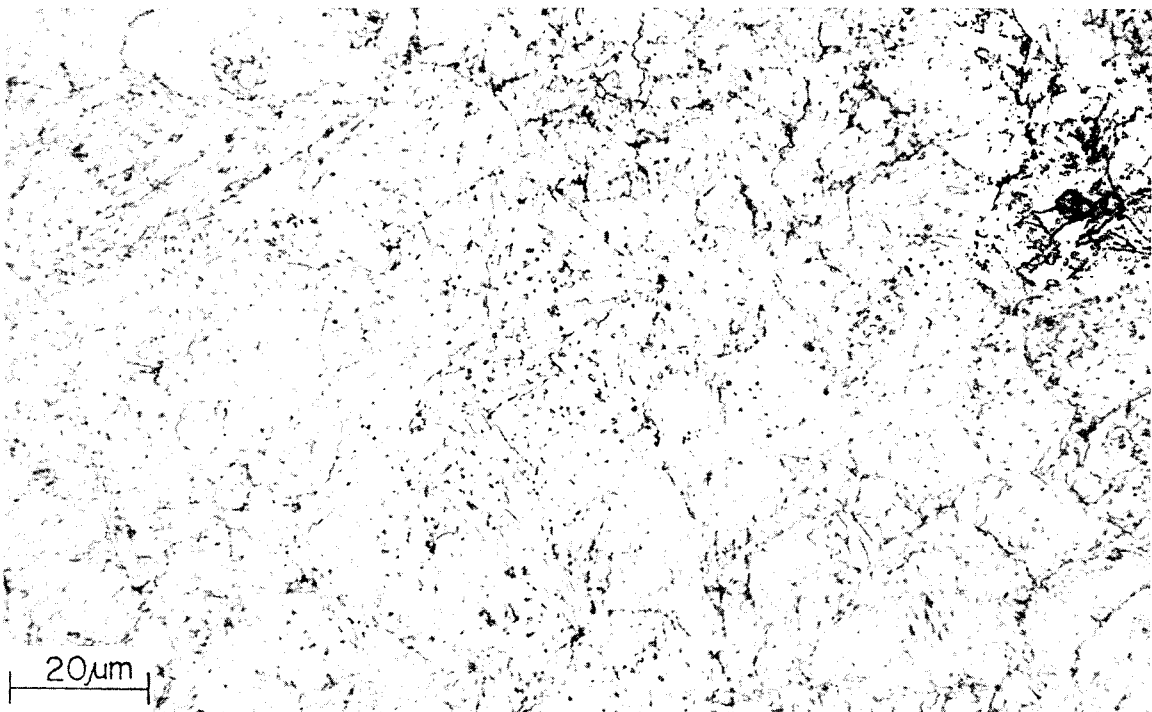


Fig. 30 — Plate-V specimen: tempered martensite containing spheroidized carbides

Code-E 10Ni-8Co (HY-180) Base Metal

The code-E specimen fractured in air showed fracture by MVC with dimples ranging from fine to coarse (Fig. 31). Stretched zones were found in conjunction with secondary cracks throughout the fracture surface, as seen in Fig. 32, but were most prevalent at the fatigue/fast-fracture interface (Fig. 33).

The hardness was 46 Rc.

The code-E specimen fractured in stress corrosion showed mixed intergranular fracture (Fig. 34) and cleavage (Fig. 35) in the SCC area. The incidence of intergranular fracture was greatest in the vicinity of the secondary cracks which had formed throughout the SCC region. The largest of these cracks occurred at the fatigue/SCC interface (Fig. 36). The fast-fracture area was characterized by MVC with a combination of small equiaxed and large conical dimples (Fig. 37).

Since both the air-break specimen and the SCC specimen had been fabricated from the as-received plate, the microstructures were the same and consisted of tempered martensite and some ferrite (Fig. 38). A heavy precipitation of carbide can be seen both within the grains and at the grain boundaries. The amount of austenite present in this material, as determined by x-ray analysis, was less than 1 percent. In the SCC specimen extensive microcracking had occurred and had originated both at the fracture edge (Fig. 39) and within the microstructure (Fig. 40).

The hardness was 45 Rc.

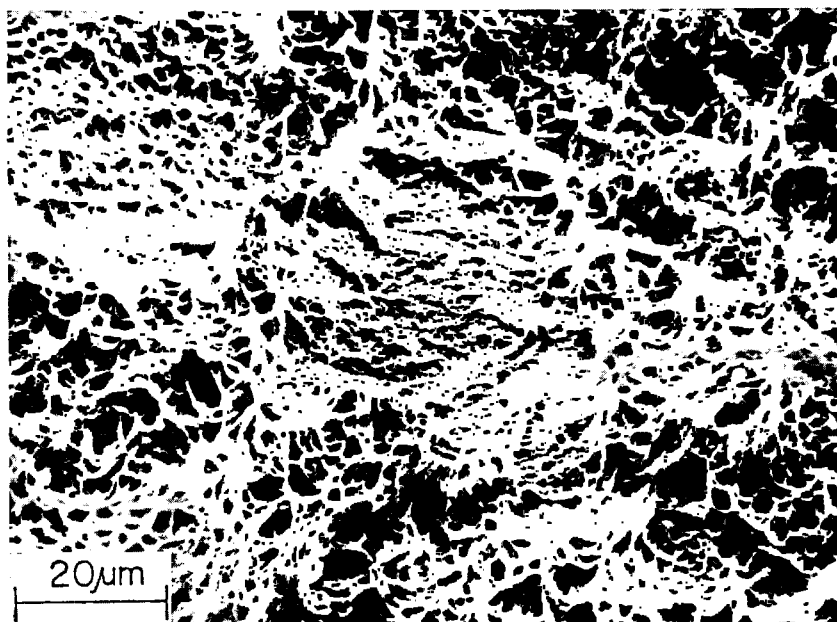


Fig. 31 — Code-E air-break specimen: MVC and mixed dimple sizes

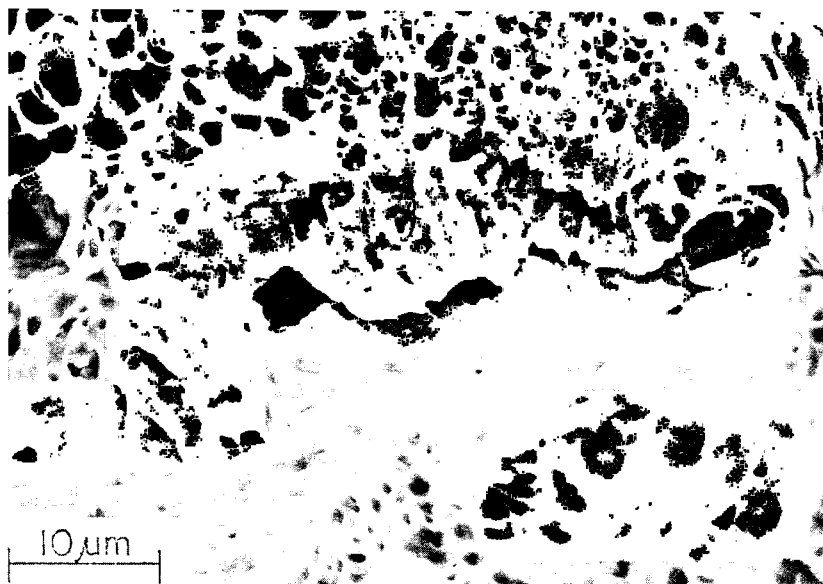


Fig. 32 — Code-E air-break specimen: stretched zones in conjunction with a secondary crack

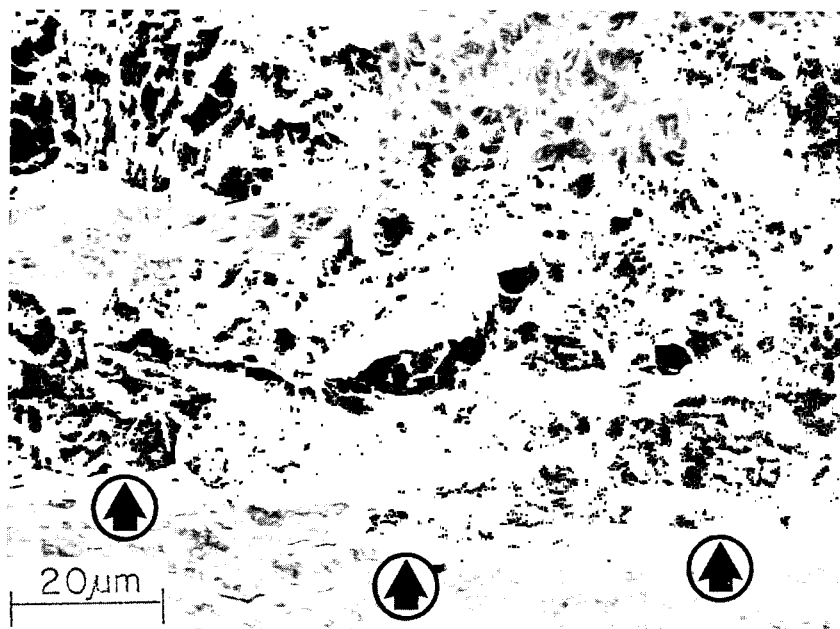


Fig. 33 — Code-E air-break specimen: stretched zones and secondary crack at the fatigue/fast-fracture interface. Arrows indicate the interface, with the fast-fracture area being above the interface.

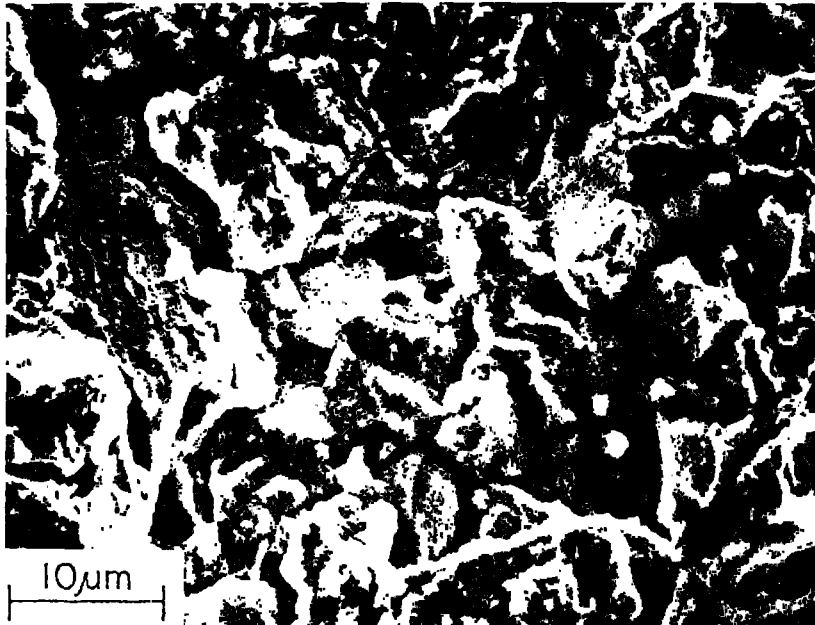


Fig. 34 — Code-E SCC specimen: intergranular fracture in the SCC area

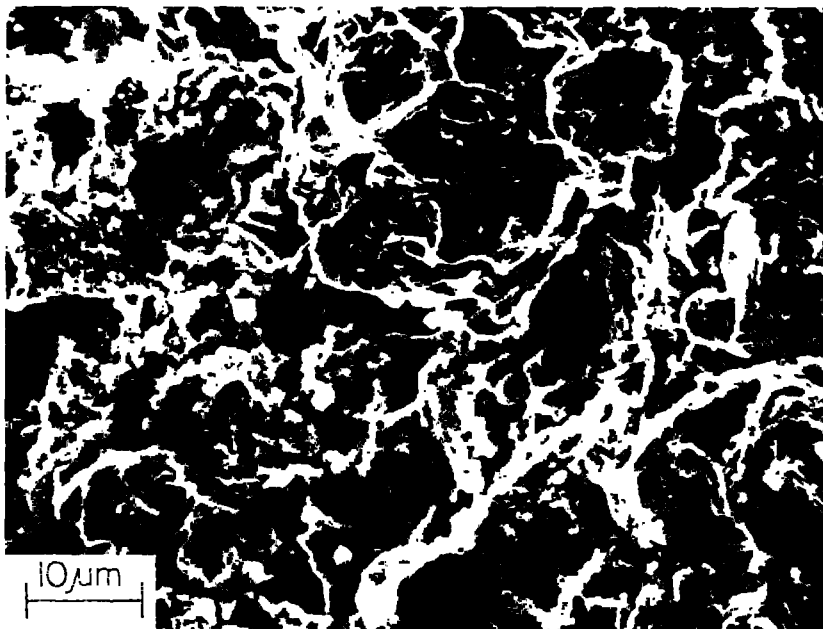


Fig. 35 — Code-E SCC specimen: cleavage in the SCC area

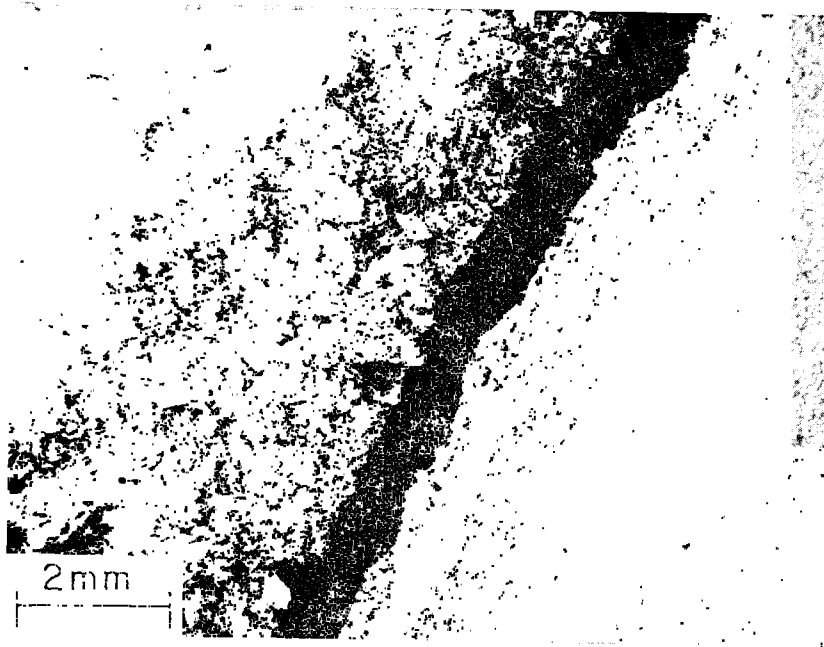


Fig. 36 — Code-E SCC specimen: a secondary crack at the fatigue/SCC interface. The SCC area is to the left of the crack.

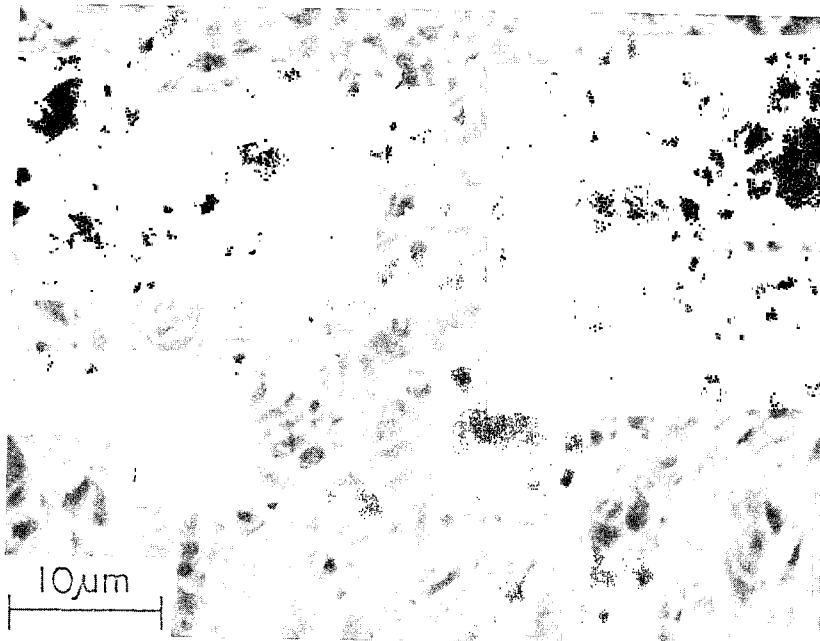


Fig. 37 — Code-E SCC specimen: MVC in the fast-fracture area and mixed dimple sizes

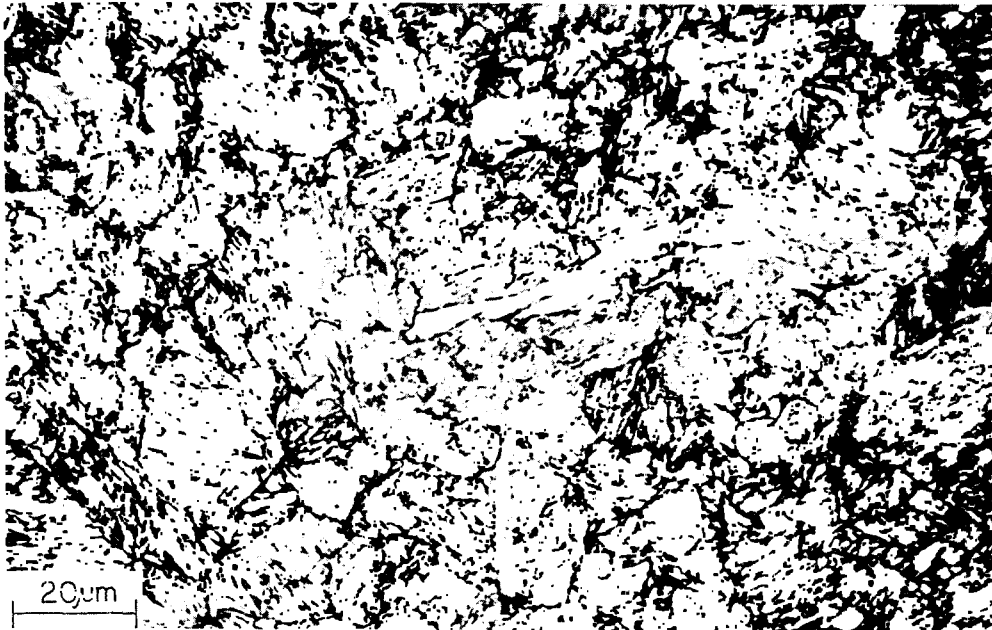


Fig. 38 — Code-E specimen: tempered martensite and ferrite

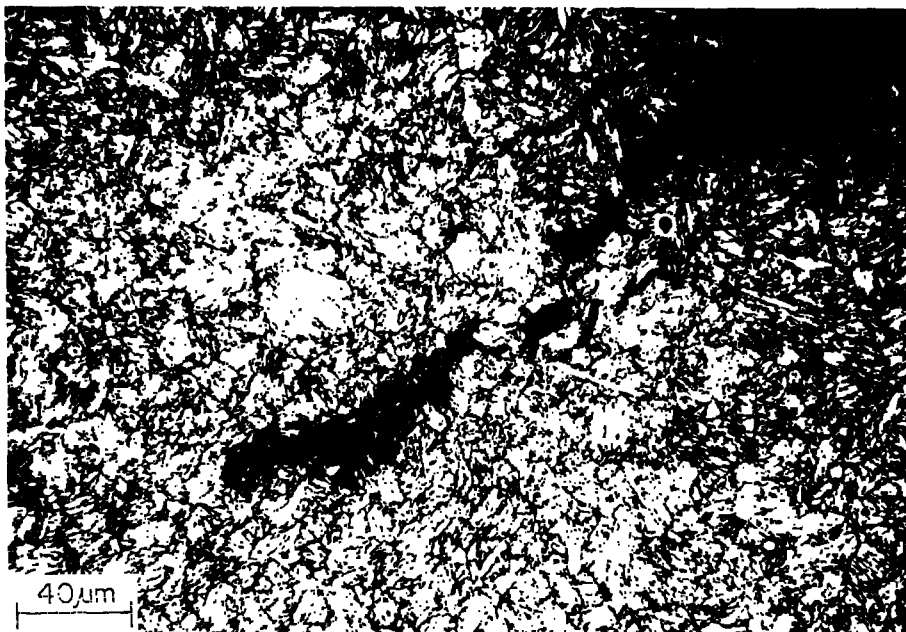


Fig. 39 — Code-E SCC specimen: microcracking at the fracture edge

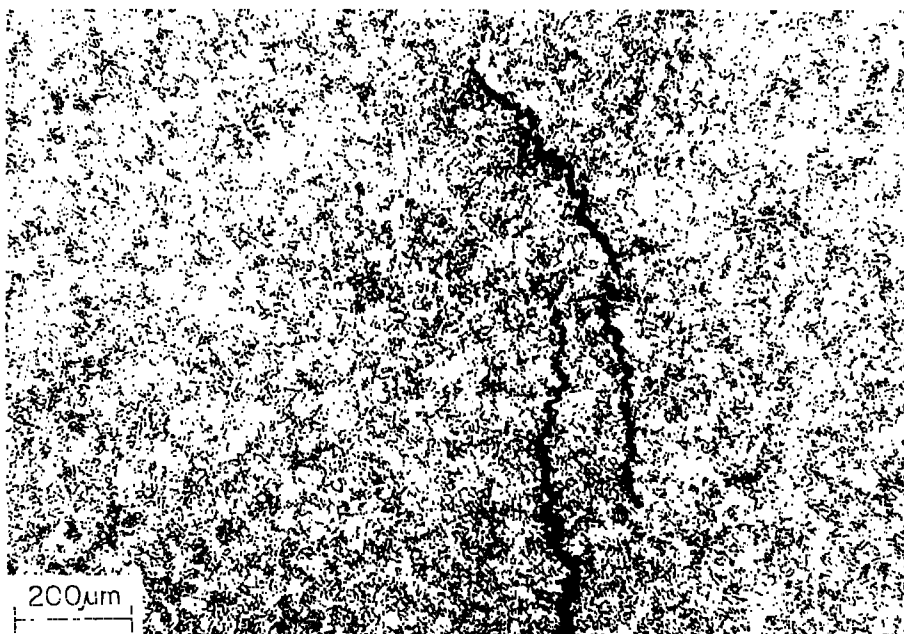


Fig. 40 — Code-E SCC specimen: microcracking originating within the microstructure

Code-D 10Ni-8Co (HY-180) Base Metal

Fracture by MVC had occurred in all of the areas examined on the fracture surface of the code-D specimen. Secondary cracking was found in both the SCC and the fast-fracture areas (Figs. 41 and 42) but was most extensive at the fatigue/SCC interface (Fig. 43). The dimples formed during fracture ranged from fine to coarse (Fig. 44), with stretched areas occurring in the vicinity of the secondary cracks (Fig. 45).

The heat treatment to which this material had been subjected resulted in the coalescing of the precipitated carbides in the martensitic microstructure, as seen in Fig. 46. The heaviest agglomeration of carbides was found at the fracture edge (Fig. 47).

The amount of retained austenite present in this specimen was about 5 percent.

Short microcracks extended from the fracture edge, and a deep crack had formed at the fatigue/SCC interface, as seen in Fig. 48. This figure also shows the presence of microvoids typical of those found throughout the specimen.

The hardness was 36 Rc.

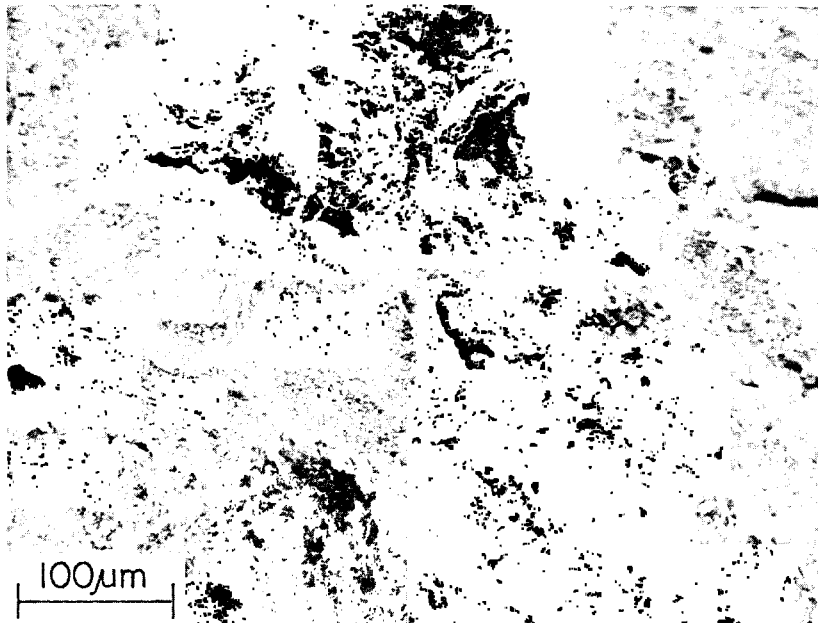


Fig. 41 — Code-D specimen: secondary cracking in the SCC area

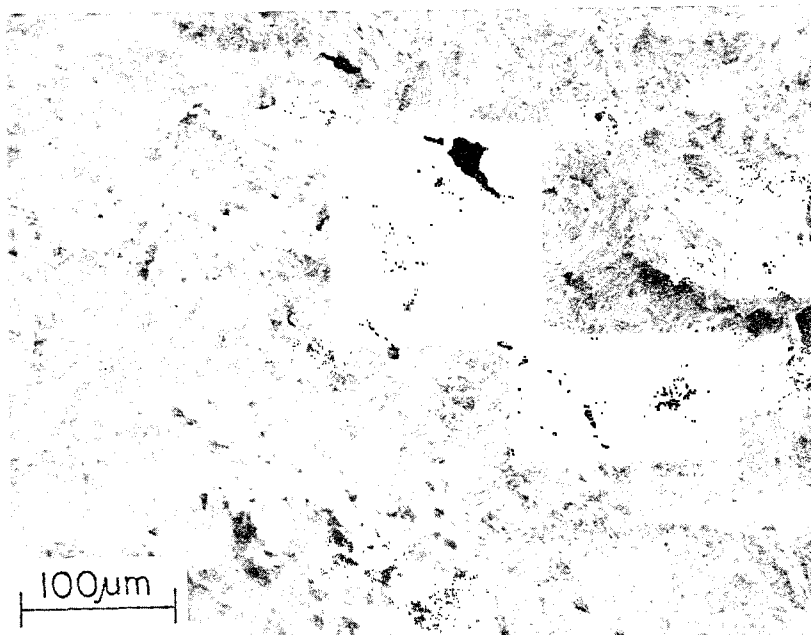


Fig. 42 — Code-D specimen: secondary cracking in the fast-fracture area

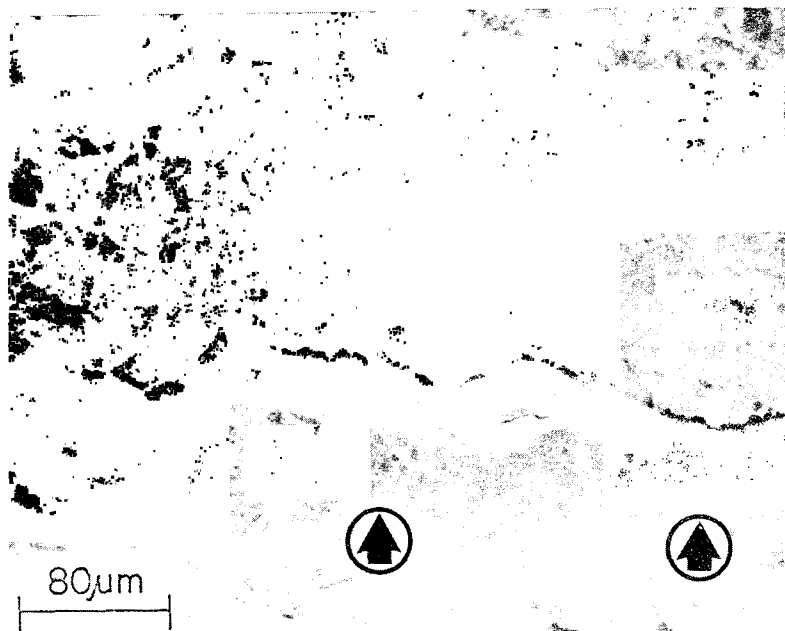


Fig. 43 — Code-D specimen: extensive secondary cracking at the fatigue/SCC interface (arrows). The SCC area is above the interface.

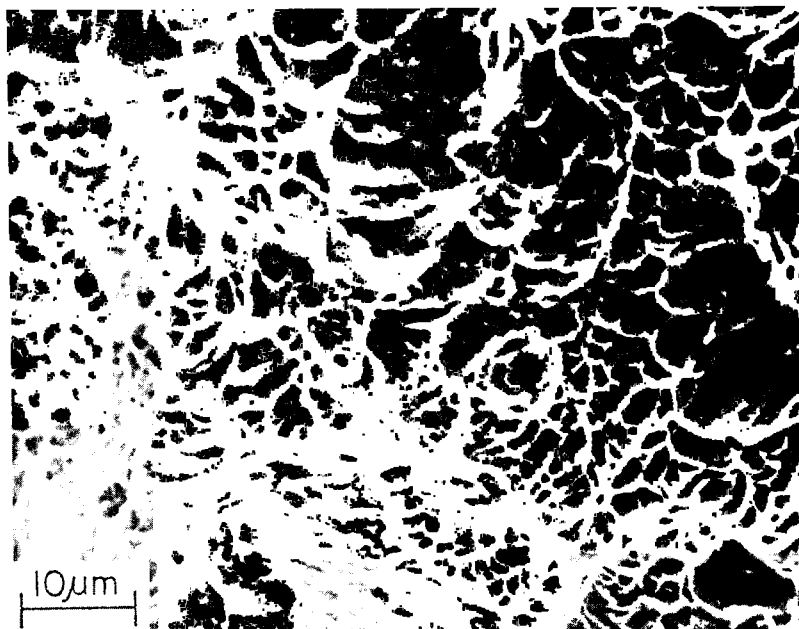


Fig. 44 — Code-D specimen: fine to coarse dimples characteristic of the SCC area

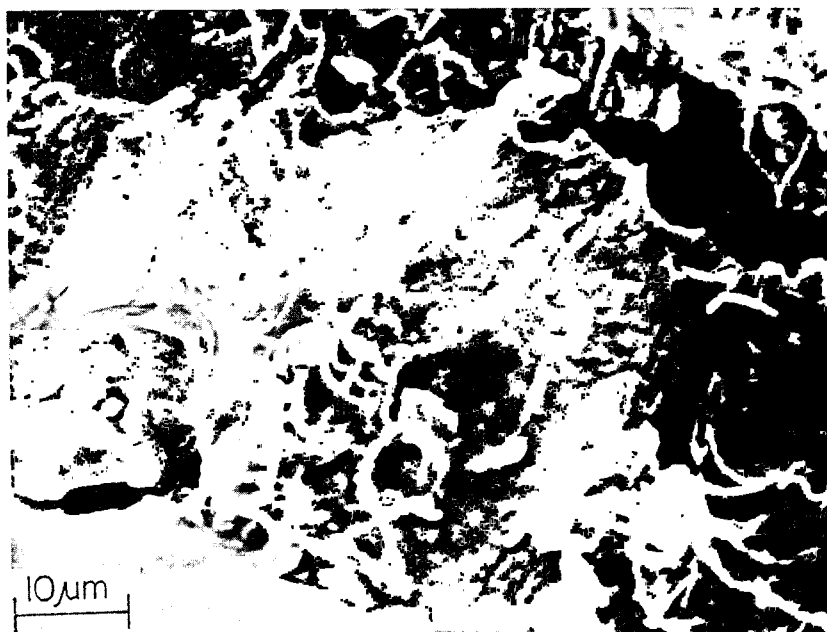


Fig. 45 — Code-D specimen: fast-fracture area showing stretching in the vicinity of the secondary cracks

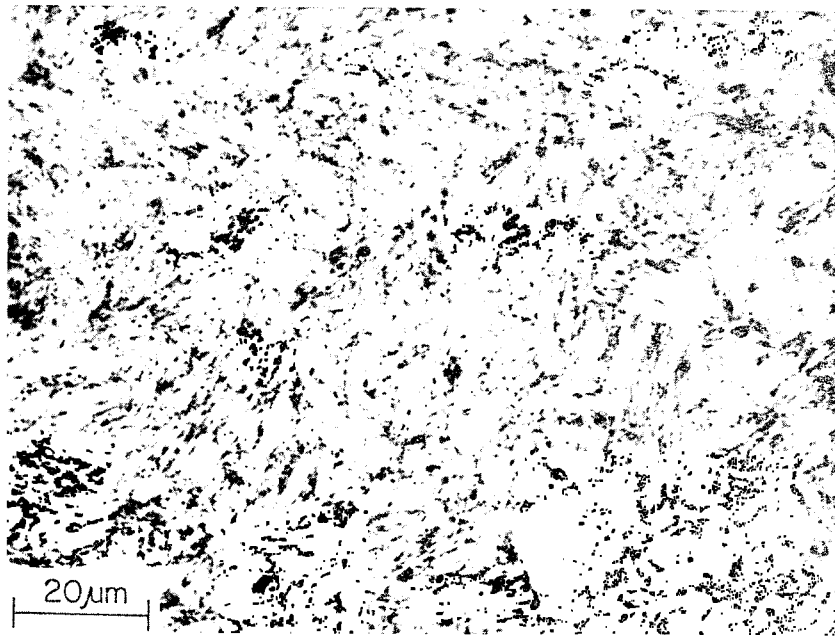


Fig. 46 — Code-D specimen: coalesced carbides in a predominately martensitic microstructure

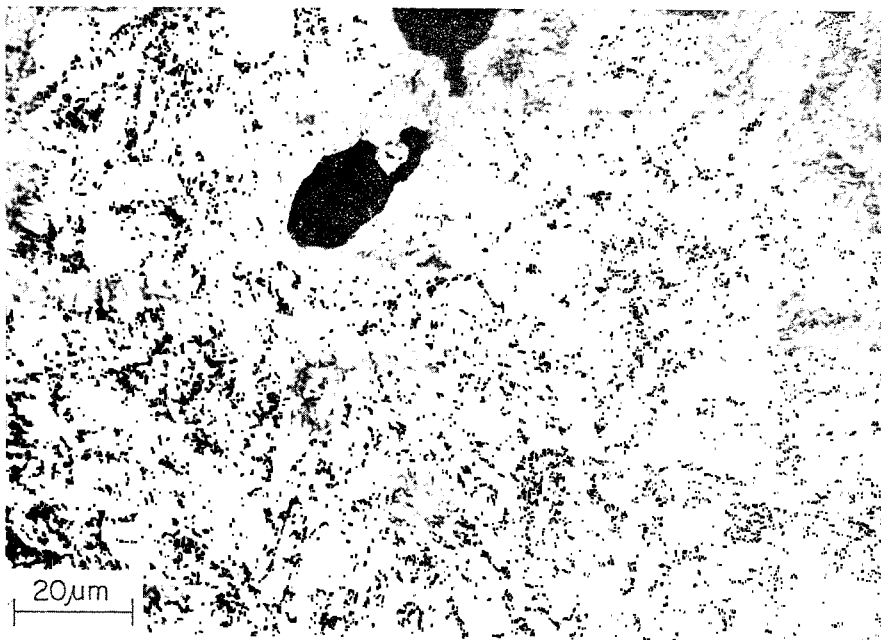


Fig. 47 — Code-D specimen: heavy agglomeration of coalesced carbides at the fracture edge

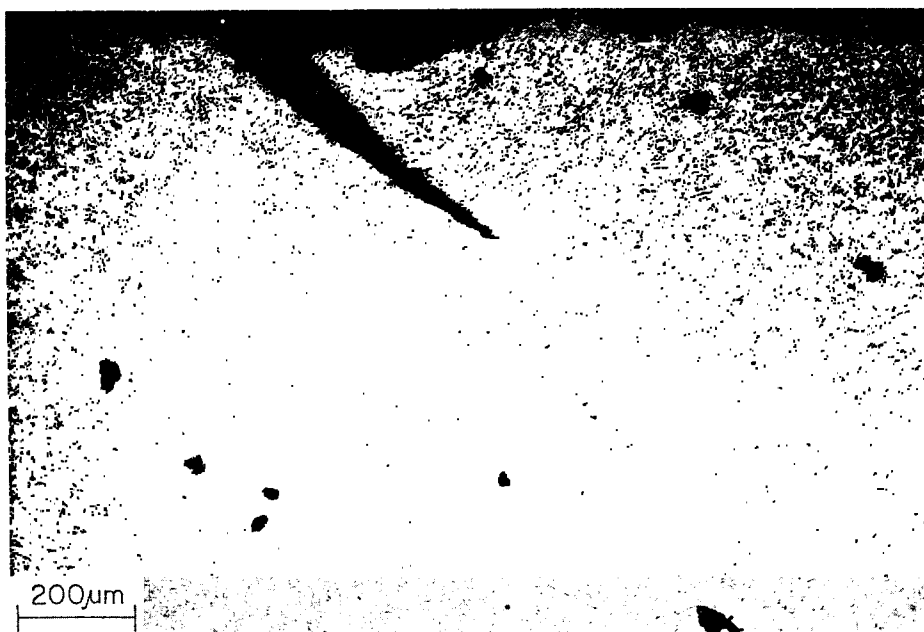


Fig. 48 — Code-D specimen: secondary crack formed at the fatigue/SCC interface and microvoids typical of those seen throughout the specimen

Code-G 9Ni-4Co Base Metal

The fracture mode in the SCC area of the code-G specimen (as-received base plate) was mixed intergranular and cleavage, with the highest incidence of intergranular fracture occurring in the vicinity of the fatigue/SCC interface (Fig. 49). Mixed cleavage and MVC characterized the fracture in the area encompassing the SCC/fast-fracture interface (Fig. 50), and in the fast-fracture area the mode was entirely MVC (Fig. 51). The dimples ranged from fine to coarse, with stretching found in areas where secondary cracking had occurred. Secondary cracking had occurred to some extent in all four areas of the fracture surface surveyed.

The microstructure was predominately tempered martensite with a heavy precipitation of carbides (Fig. 52). In some areas chainlike formations of the carbide precipitates had formed along grain boundaries. The amount of retained austenite in the code-G material was approximately 1 percent.

Extensive microcracking had occurred at the fracture edge and within the specimen interior (Fig. 53). The microcracks were discontinuous and in some instances could be identified as grain-boundary cracks coinciding with the carbide chains (Fig. 54).

The hardness was 44 Rc.

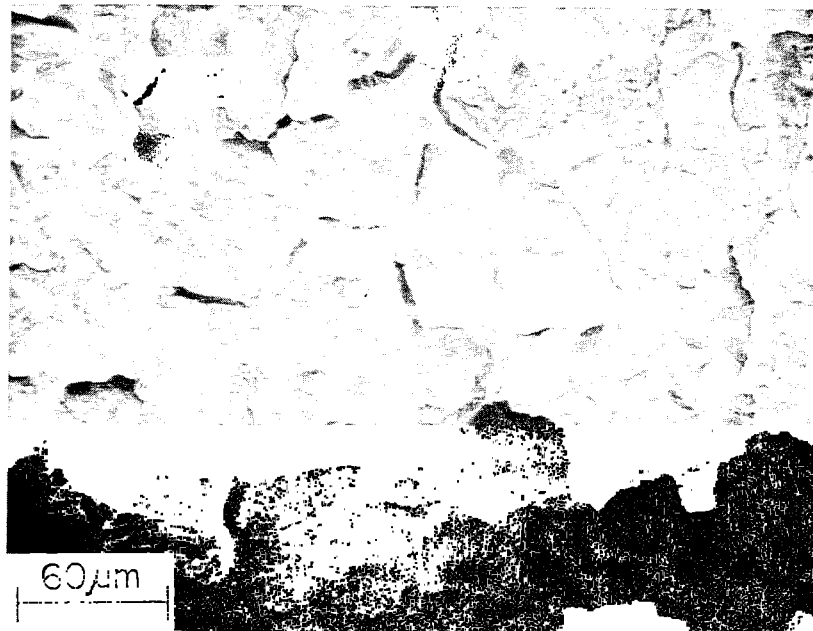


Fig. 49 — Code-G specimen: intergranular fracture in the vicinity of the fatigue/SCC interface

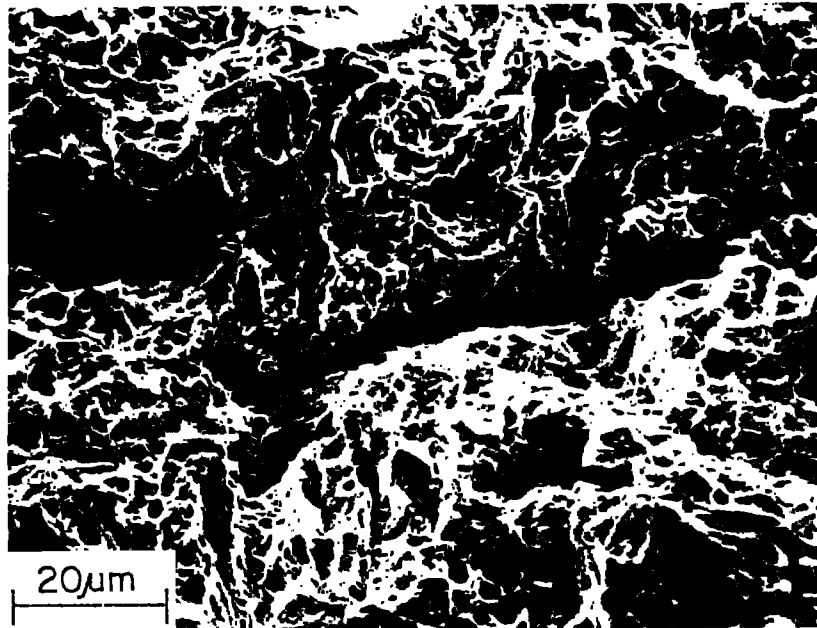


Fig. 50 — Code-G specimen: MVC, cleavage, and secondary cracking in the area encompassing the SCC/fast-fracture interface

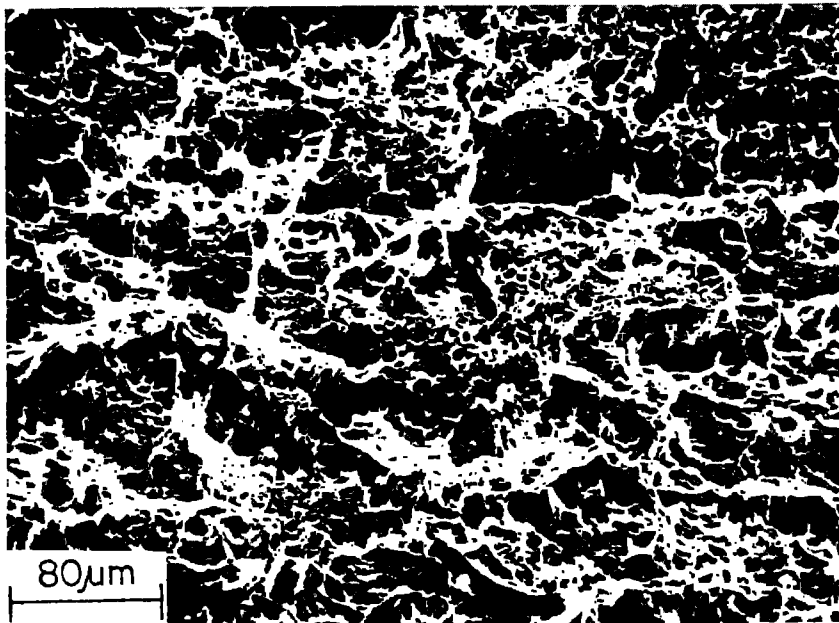


Fig. 51 — Code-G specimen: fast-fracture area showing MVC and stretched zones associated with secondary cracking

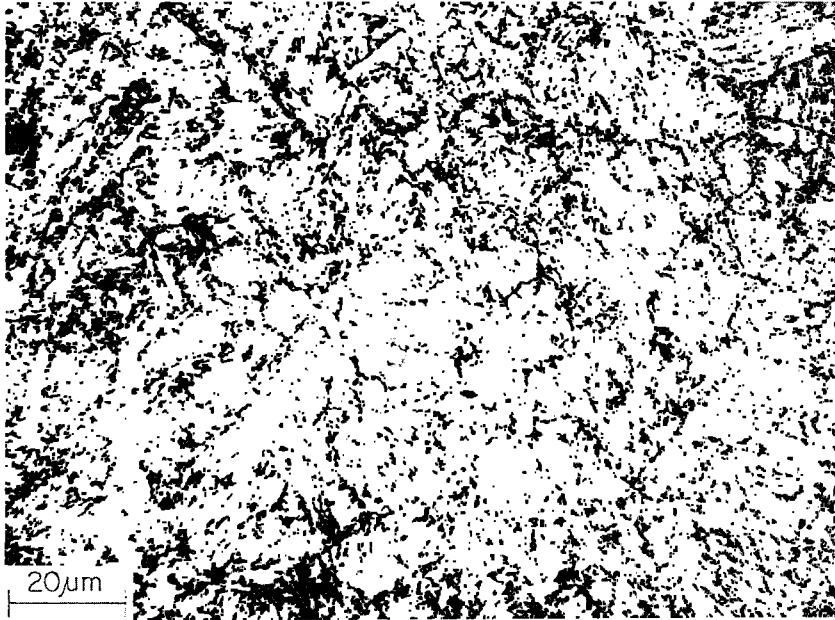


Fig. 52 — Code-G specimen: tempered martensite containing a heavy precipitation of carbides



Fig. 53 — Code-G specimen: microcracking at the fracture edge and within the interior of the specimen

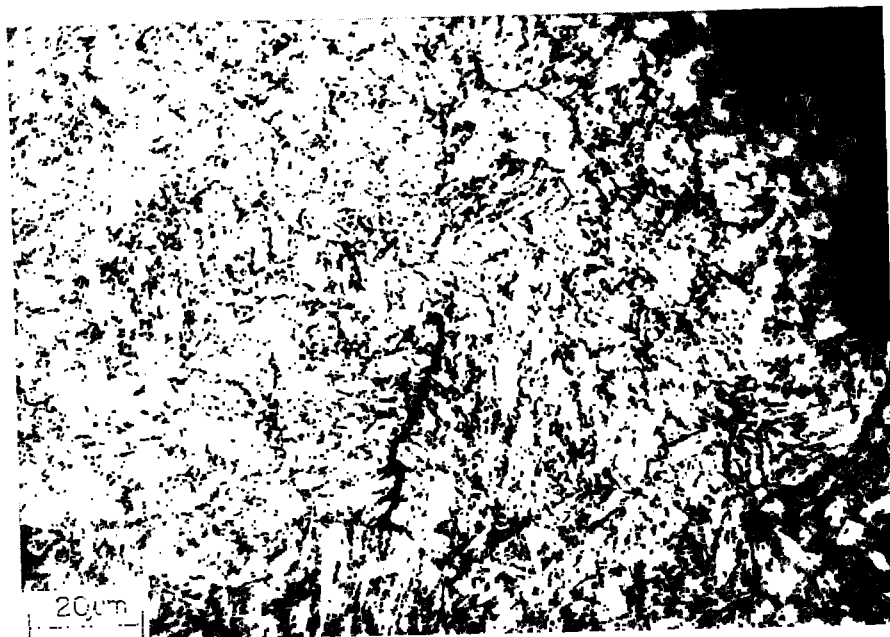


Fig. 54 — Code-G specimen: microcracks along grain boundaries and through precipitated carbides

Code-F 9Ni-4Co Base Metal

The code-F specimen (tempered base plate) showed fracture by MVC in both the SCC and the fast-fracture areas (Figs. 55 and 56), with cleavage occurring in the regions of secondary cracking (Fig. 57).

The microstructure developed upon overaging was a combination of highly tempered martensite, bainite, and retained austenite (Fig. 58). The bainitic structure is seen at higher magnification in Fig. 59. The amount of retained austenite in this specimen was approximately 8 percent.

The hardness was 34 to 37 Rc.

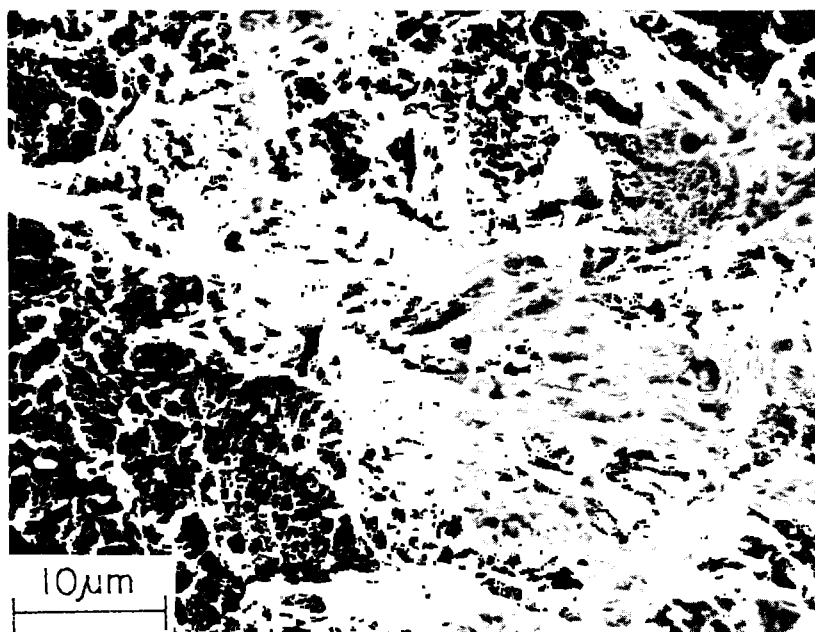


Fig. 55 — Code-F specimen: MVC in the SCC area

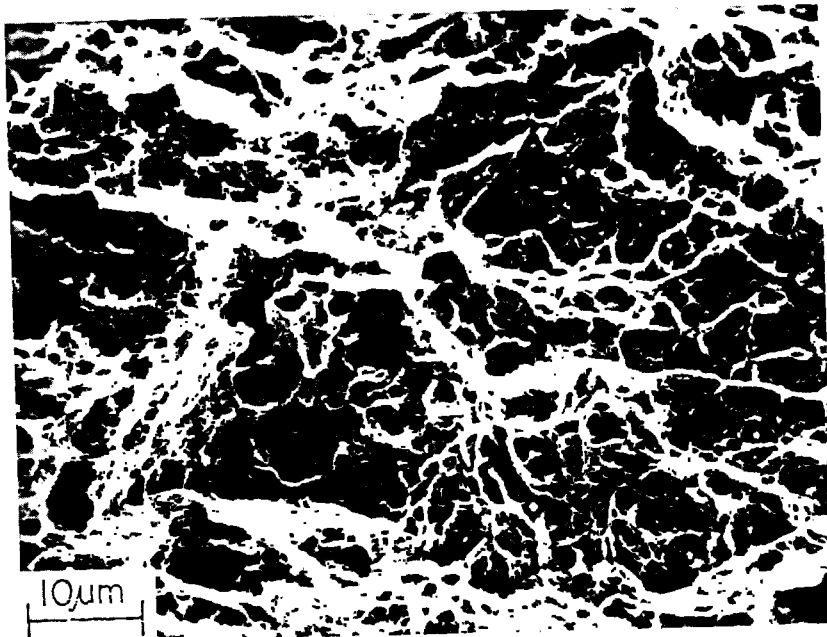


Fig. 56 — Code-F specimen: MVC in the fast-fracture area

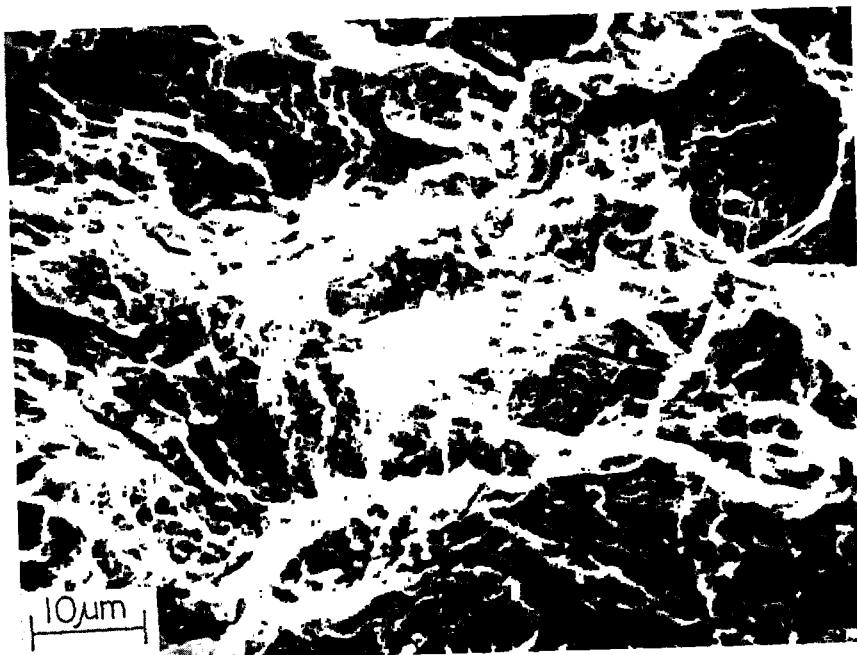


Fig. 57 — Code-F specimen: cleavage seen in conjunction with secondary cracks

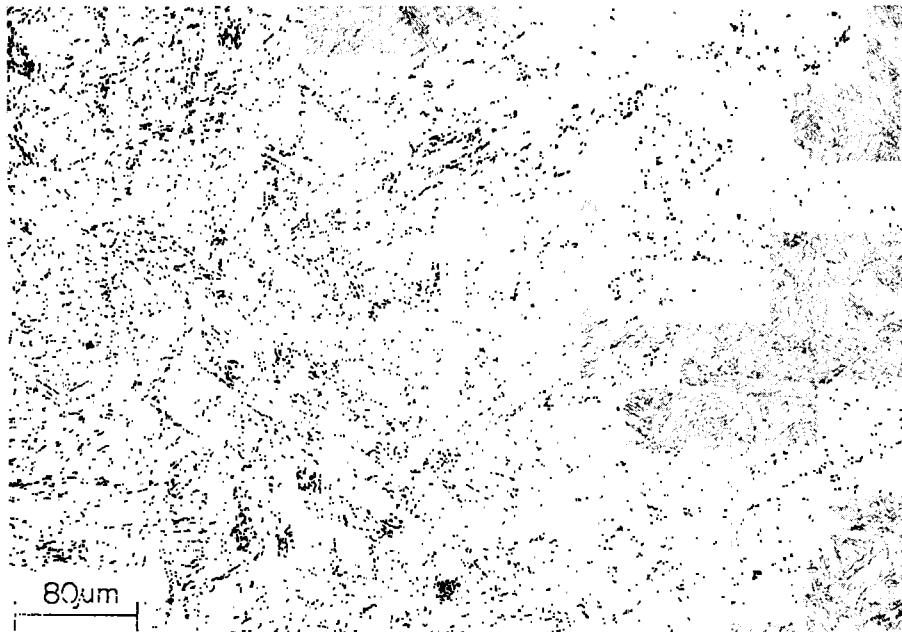


Fig. 58 — Code-F specimen: highly tempered martensite and bainite

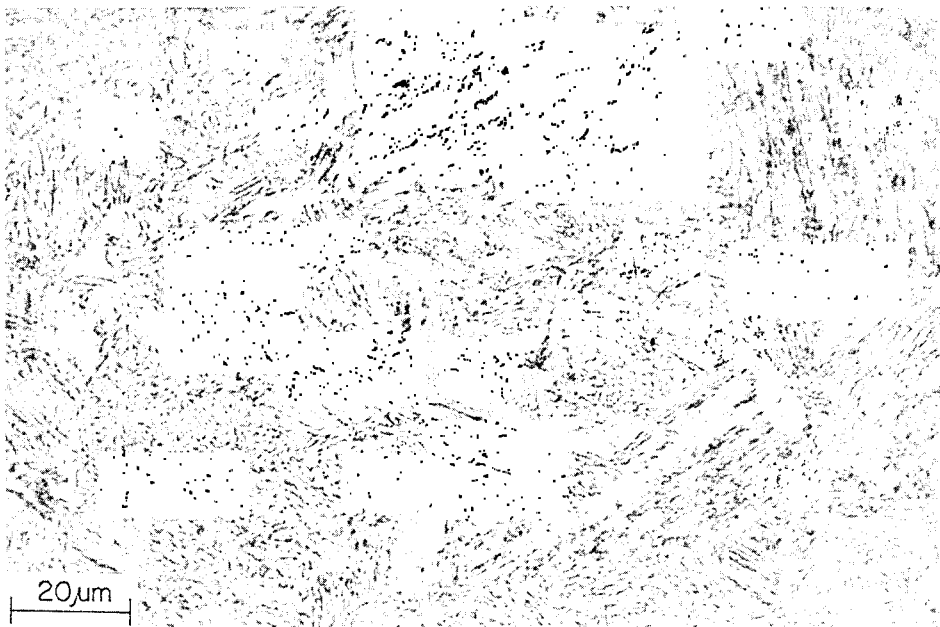


Fig. 59 — Code-F specimen: bainite at higher magnification than in Fig. 58

DISCUSSION

Materials composed of a fine, tempered martensitic microstructure and a relatively uniform grain size offer the greatest resistance to SCC in the HY-130 system.

Of the two base plates analyzed in the as-received condition, the specimen with the more uniform microstructure (code B) showed higher resistance to SCC. Transgranular fracture by MVC with little secondary cracking in the SCC area and virtually none at the fatigue/SCC interface indicates relatively little embrittlement of this specimen during stress-corrosion testing.

The high degree of resistance to SCC exhibited by plate V appears to be related to the uniformity of its microstructure. Although some embrittlement of this specimen was seen in minor amounts of cleavage in the SCC area, the high $K_{I_{SCC}}$ value reported suggests that the degree of refinement of the microstructure is of overriding importance.

The heat treatments to which the code-C and code-H materials were subjected (tempering at 510°C and 566°C (950°F and 1050°F) respectively) resulted in recrystallization, as seen in the greater uniformity of microstructure as compared to the as-received plate (code A). The microstructure of the code-H material was slightly coarser than that of the code-C material. The air cooling of the code-C material after tempering led to spheroidization of the carbides with some embrittlement, as seen in the increased amount of fracture by cleavage throughout the code-C specimen as compared to the code-A specimen. The quenching of the code-H material after tempering resulted in more severe embrittlement, as evidenced by the occurrence of intergranular fracture, in addition to cleavage, in the SCC area.

The extreme variations in hardness in the code-C material (31 to 37 Rc), due to the irregular and severe banding of this specimen, may have contributed to rapid failure during stress-corrosion testing and to the mixed ductile-brittle fracture mode seen in the fast-fracture area.

The highly tempered microstructure containing coalesced carbides, produced by overaging the 10Ni-8Co plate, resulted in increased resistance to SCC, whereas the mixed martensitic-bainitic microstructure, which resulted from overaging the 9Ni-4Co plate, led to a slight reduction in SCC resistance. Both specimens in the overaged condition showed increased ductility on the micro scale and fewer secondary cracks as compared to the as-received plate.

ACKNOWLEDGMENTS

The x-ray analysis of the 10Ni-8Co and 9Ni-4Co specimens by Mr. P. W. Holsberg of the David W. Taylor Naval Ship Research and Development Center, Annapolis, Maryland, and the performance of all SCC tests by Mr. R. L. Newbegin of the Naval Research Laboratory are gratefully acknowledged. The work was financially supported by the Naval Sea Systems Command (SEA 035).

REFERENCES

1. B.F. Brown, "A New Stress-Corrosion Cracking Test for High Strength Alloys," *Materials Research and Standards* 6 (No. 3), 129-133 (1966).
2. J.A. Kies, H.L. Smith, H.E. Romine, and H. Bernstein, "Fracture Testing of Weldments," pp. 328-356 in *Fracture Toughness Testing and Its Application*, ASTM STP 381, American Society for Testing and Materials, Philadelphia, 1965.
3. W.E. King, "Load Crack Testing Device," U.S. Patent 3,965,729 (June 29, 1976).
4. C.T. Fujii and E.A. Metzbower, "The SCC Properties of HY-130 Steel Plate and Weldments," NRL Memorandum Report 3463, Mar. 1977.
5. C.T. Fujii, "Stress-Corrosion Cracking Properties of 17-4 PH Steel," pp. 213-225 in *Stress-Corrosion—New Approaches*, ASTM STP 610, American Society for Testing and Materials, Philadelphia, 1976.

Appendix A

CHEMICAL COMPOSITION AND TENSILE PROPERTIES

OF THE MATERIALS

Tables A1 through A4 give the chemical composition and tensile properties of the materials selected for the tests (Figs. 1 and 2).

Table A1 — Chemical Composition of Base Metals (Data from David W. Taylor
Naval Ship Research and Development Center, Annapolis Laboratory, Code 2821)

Material	Code	Chemical Analysis (wt-%)							
		C	Mn	P	S	Si	Cu	Ni	
HY-130/EF HY-130/ESR HY-130/EF 10Ni-8Co 9Ni-4Co	A, C, H	0.11	0.76	0.005	0.004	0.31	0.022	5.00	
	B	0.10	0.80	0.006	0.005	0.14	0.120	5.09	
	V	0.10	0.76	0.004	0.004	0.26	0.21	4.97	
	D, E	0.13	0.14	0.003	0.004	0.054	<0.02	10.00	
	F, G	0.21	0.15	0.006	0.005	0.074	<0.02	8.80	
	</								

Table A2 — Chemical Composition of Deposited Weld Metals (Data from David W. Taylor
Naval Ship Research and Development Center, Annapolis Laboratory, Code 2821)

Electrode/ Process	Code	Chemical Analysis (wt-%)							
		C	Mn	P	S	Si	Cu	Ni	
Linde/GMA Linde/GTA Airco/GMA Airco/GTA HY-130/GMA HY-130/GTA McKay/SMA HY-180/GTA	C, D, L	0.11	1.32	0.004	0.003	0.32	0.039	2.81	
	F	0.13	1.43	0.004	0.003	0.35	0.037	2.97	
	R	0.093	1.50	0.009	0.007	0.31	0.057	2.59	
	S	0.11	1.47	0.007	0.005	0.33	0.047	2.78	
	G, K	0.083	0.69	0.006	0.002	0.23	0.17	4.99	
	T	0.077	0.78	0.005	0.001	0.25	0.13	4.88	
	E	0.064	1.16	0.009	0.003	0.45	0.02	3.80	
	H, I, J, Q	0.12	0.11	0.007	0.004	0.11	<0.02	9.90	
		Cr	Mo	V	Ti	Co	N	O	
	C, D, L	0.60	0.84	0.010	0.016	0.02	0.006	0.0167	
	F	0.67	0.83	0.011	0.022	0.02	0.006	0.0010	
	R	0.91	0.61	0.016	0.012	—	0.006	0.0205	
	S	0.82	0.60	0.030	0.012	0.02	0.007	0.0017	
	G, K	0.56	0.49	0.063	0.007	—	0.012	0.0400	
	T	0.56	0.48	0.059	0.008	—	0.007	0.0012	
	E	0.58	0.85	0.019	0.014	—	0.011	0.0266	
	H, I, J, Q	2.32	1.02	0.058	<0.01	8.20	0.005	0.0008	

Table A3 — Tensile Properties of Base Metals (Data from David W. Taylor
Naval Ship Research and Development Center, Annapolis Laboratory, Code 2821)

Material	Condition	Code	0.2% Yield Strength, σ_{ys}		Ultimate Tensile Strength, σ_{uts}		Elonga- tion, El (%)	Reduction in Area, RA (%)
			(MPa)	(ksi)	(MPa)	(ksi)		
HY-130/EF	As received	A	938	136	979	142	21	55
HY-130/EF	Heat treated	C	910	132	965	140	16	57
HY-130/EF	Heat treated	H	1027	149	1103	160	19	63
HY-130/ESR	As received	B	986	143	1007	146	19	61
10Ni-8Co	As received	E	1282	186	1469	213	19	61
10Ni-8Co	Heat treated	D	952	138	1083	157	22	74
9Ni-4Co	As received	G	1282	186	1365	198	19	67
9Ni-4Co	Heat treated	F	786	114	1269	184	18	51

Table A4 — Tensile Properties of Deposited Weld Metals (Data from David W. Taylor
Naval Ship Research and Development Center, Annapolis Laboratory, Code 2821)

Electrode/ Process	Condition	Code	0.2% Yield Strength, σ_{ys}		Ultimate Tensile Strength, σ_{uts}		Elonga- tion, El (%)	Reduction in Area, RA (%)
			(MPa)	(ksi)	(MPa)	(ksi)		
Linde/GMA	As welded	C	869	126	965	140	22	70
Linde/GMA	As welded	D	993	144	1055	153	19	68
Linde/GTA	As welded	F	1041	151	1048	152	25	78
Linde/GMA	Heat treated	L	1000	145	1062	154	17	36
Airco/GMA	As welded	R	1034	150	1096	159	17	64
Airco/GTA	As welded	S	1041	151	1055	153	22	72
HY-130/GMA	As welded	G	938	136	993	144	16	52
HY-130/GMA	Heat treated	K	903	131	958	139	11	21
HY-130/GTA	As welded	T	1048	152	1048	152	25	78
McKay/SMA	As welded	E	993	144	1034	150	18	66
HY-180/GTA	As welded	I	1138	165	1441	209	18	65
HY-180/GTA	As welded	J	1296	188	1455	211	19	71
HY-180/GTA	Heat treated	H	862	125	1145	166	20	71
HY-180/GTA	Heat treated	Q	1331	193	1400	203	20	72

